

S⁴N: A spectroscopic survey of stars in the solar neighborhood^{★,★★}

The Nearest 15 pc

C. Allende Prieto¹, P. S. Barklem², D. L. Lambert¹, and K. Cunha³

¹ McDonald Observatory and Department of Astronomy, University of Texas, Austin, TX 78712-1083, USA
e-mail: d1l@astro.as.utexas.edu

² Uppsala Astronomical Observatory, Box 515, 751-20 Uppsala, Sweden
e-mail: barklem@astro.uu.se

³ Observatório Nacional, Rua General José Cristino 77 CEP 20921-400, Rio de Janeiro, Brazil
e-mail: katia@on.br

Received 4 December 2003 / Accepted 3 March 2004

Abstract. We report the results of a high-resolution spectroscopic survey of all the stars more luminous than $M_V = 6.5$ mag within 14.5 pc from the Sun. The *Hipparcos* catalog's completeness limits guarantee that our survey is comprehensive and free from some of the selection effects in other samples of nearby stars. The resulting spectroscopic database, which we have made publicly available, includes spectra for 118 stars obtained with a resolving power of $R \approx 50\,000$, continuous spectral coverage between $\sim 362\text{--}921$ nm, and typical signal-to-noise ratios in the range 150–600. We derive stellar parameters and perform a preliminary abundance and kinematic analysis of the F-G-K stars in the sample. The inferred metallicity ([Fe/H]) distribution is centered at about -0.1 dex, and shows a standard deviation of 0.2 dex. A comparison with larger samples of *Hipparcos* stars, some of which have been part of previous abundance studies, suggests that our limited sample is representative of a larger volume of the local thin disk. We identify a number of metal-rich K-type stars which appear to be very old, confirming the claims for the existence of such stars in the solar neighborhood. With atmospheric effective temperatures and gravities derived independently of the spectra, we find that our classical LTE model-atmosphere analysis of metal-rich (and mainly K-type) stars provides discrepant abundances from neutral and ionized lines of several metals. This ionization imbalance could be a sign of departures from LTE or inhomogeneous structure, which are ignored in the interpretation of the spectra. Alternatively, but seemingly unlikely, the mismatch could be explained by systematic errors in the scale of effective temperatures. Based on transitions of majority species, we discuss abundances of 16 chemical elements. In agreement with earlier studies we find that the abundance ratios to iron of Si, Sc, Ti, Co, and Zn become smaller as the iron abundance increases until approaching the solar values, but the trends reverse for higher iron abundances. At any given metallicity, stars with a low galactic rotational velocity tend to have high abundances of Mg, Si, Ca, Sc, Ti, Co, Zn, and Eu, but low abundances of Ba, Ce, and Nd. The Sun appears deficient by roughly 0.1 dex in O, Si, Ca, Sc, Ti, Y, Ce, Nd, and Eu, compared to its immediate neighbors with similar iron abundances.

Key words. surveys – stars: fundamental parameters – stars: abundances – Galaxy: solar neighbourhood

1. Introduction

The study of the stellar population of the solar neighborhood is of interest for a wide range of investigations. Nearby stars are

Send offprint requests to: C. Allende Prieto,
e-mail: callende@astro.as.utexas.edu

* Based on observations made with the 2.7 m telescope at the McDonald Observatory of the University of Texas at Austin (Texas), and the 1.52 m telescope at the European Southern Observatory (La Silla, Chile) under the agreement with the CNPq/Observatório Nacional (Brazil).

** Tables 3–5 are only available in electronic form at the CDS via anonymous ftp to cdsarc.u-strasbg.fr (130.79.128.5) or via <http://cdsweb.u-strasbg.fr/cgi-bin/qcat?J/A+A/420/183>

the only ones for which we can obtain crucial measurements, such as parallaxes or angular diameters. They are typically the best candidates for very precise spectroscopic followups, such as searches for lower-mass companions (stellar, brown dwarf, or planetary), circumstellar disks, or solar-like cycles. Their proximity involves obvious advantages that should be exploited.

From a wider perspective, the stellar population of the solar neighborhood may be representative of larger parts of the Galactic disk. Early studies revealed that the simplest models of Galactic chemical evolution could not match the observed metallicity distribution – the so-called G-dwarf problem (van den Bergh 1962). Recent investigations have shown

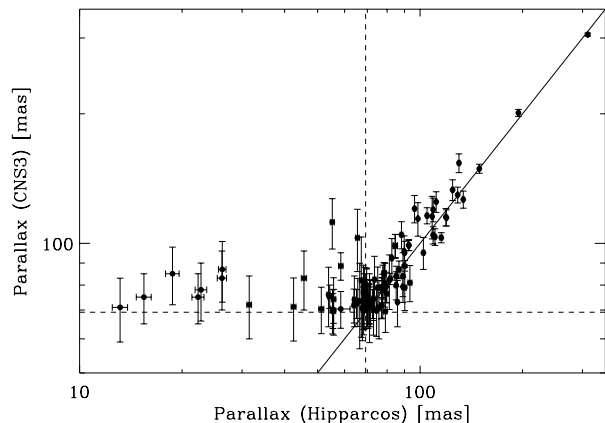


Fig. 1. Comparison of the parallaxes larger than 69.18 mas included in CNS3, against *Hipparcos*. *Hipparcos* has revealed that a significant fraction of these stars are indeed further away from the Sun. The solid straight line has a slope of one.

that more complex scenarios, such as those including inhomogeneous evolution (Malinie et al. 1993) or infall (Chiappini et al. 1997), more closely resemble the observations. However, almost all the derived metallicity distributions of samples approximately limited in volume, have been obtained from photometry (Twarog 1980; Rocha-Pinto & Maciel 1996, 1998a; Flynn & Morell 1997; Kotoneva et al. 2002). This is worrying, as it has been recognized that some of the employed photometric indices may be seriously affected by chromospheric activity (Rocha-Pinto & Maciel 1998b; Favata et al. 1997a) and other systematic effects (Haywood 2002; Reid 2002; Twarog et al. 2002). These uncertainties can be avoided by using spectra. Favata et al. (1997b) carried out the only existing spectroscopic study of a volume-limited sample of nearby stars, and found a metallicity distribution for K dwarfs which is remarkably more metal-rich than those obtained through photometric analyses.

We have conducted a complete M_V -limited volume-limited survey of nearby stars in an attempt to settle these and other issues. In addition to the Catalogue of Nearby Stars (Gliese & Jahreiß 1991, hereafter CNS3) – used by most of the previous studies – we have taken advantage of the *Hipparcos* catalog (ESA 1997). *Hipparcos* is complete down to $V = 7.3^1$. Restricting the study to stars brighter than $M_V = 6.5$ ($\approx K2V$), *Hipparcos*' completeness reaches out to 14.5 pc. Figure 1 shows that nearly 25% of the stars included in CNS3 within 14.5 pc from the Sun (parallaxes larger than 69.18 mas) are in fact farther away according to the accurate parallaxes measured by *Hipparcos*.

High-dispersion high signal-to-noise optical spectra were acquired for 118 stars: all the objects more luminous than $M_V = 6.5$ within 14.5 pc from the Sun. Figure 2 shows the sample's distribution of absolute and visual V magnitudes: M_V (solid line) and V (dashed line). As a reference, spectral types for dwarfs are assigned to different ranges in M_V . This sample, as a result of the dependence of stellar lifetime on mass and the shape of the initial mass function, is dominated by the

¹ This is a lower limit; the actual values depend on galactic latitude and spectral type.

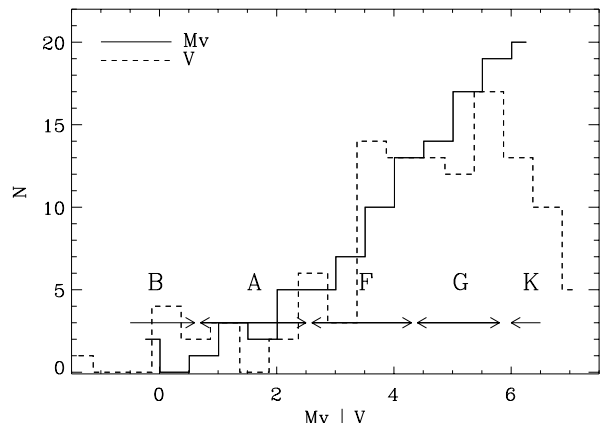


Fig. 2. Distribution of absolute (M_V ; solid line) and visual (V ; dashed line) magnitudes of the sample. Approximate spectral types for dwarfs are assigned to the different ranges of M_V as reference.

Table 1. Observations.

Observatory	Dates
La Silla	October 2000
McDonald	December 2000
McDonald	April–May 2001
La Silla	May 2001
McDonald	September 2001
La Silla	September 2001
McDonald	October 2001
La Silla	November 2001

coolest stars within our range of spectral types. This should be borne in mind when comparing to most other high-resolution spectroscopic studies of disk stars, which tend to select warmer targets.

We provide a high-quality spectroscopic archive of these *nearest* stars. The data acquisition, reduction and archival, are the subject of Sect. 2. Many properties of these stars have been compiled: radial velocities, parallaxes, and proper motions. Other properties have been determined afresh: stellar atmospheric parameters, kinematics, ages, and chemical abundances. The resulting catalog is described in Sect. 3. Section 4 examines the consistency of the inferred abundances. Section 5 discusses our findings. Section 6 compares the kinematics and metallicities of the nearest stars with larger samples of thin-disk stars, and Sect. 7 presents a short summary and provides suggestions for future work.

2. Observations, data processing, and final archive

The observations were obtained with the Harlan J. Smith 2.7 m telescope at McDonald Observatory and the ESO 1.52 m telescope on La Silla. The spectra have a resolving power of $\sim 5 \times 10^4$, fully cover the optical range, and extend into the near IR. A total of eight observing campaigns were necessary, as summarized in Table 1.

The McDonald spectra were obtained with the 2dcoudé spectrograph (Tull et al. 1995). This cross-dispersed echelle spectrograph provides, in a single exposure, full coverage from

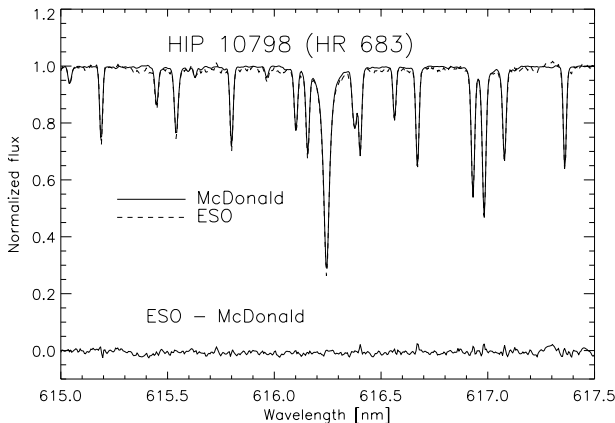


Fig. 3. Continuum corrected spectra of HIP 10798 obtained with the 2dcoude spectrograph on the 2.7 m telescope at McDonald Observatory and the FEROS spectrograph on the 1.52 m telescope at ESO. The McDonald spectrum has been convolved with a 1.5 pixels *FWHM* Gaussian to compensate for the higher resolution of the 2dcoude observations. The difference between the two spectra is also shown with a solid line (meandering about zero).

about 360 nm to \sim 510 nm, but has increasingly larger gaps between redder orders. This problem was circumvented by using two different overlapping settings. The detector was TK3, a thinned 2048 \times 2048 Tektronix CCD with 24 μ m pixels, which was installed at the F3 focus. We used grating E2, a 53.67 gr mm⁻¹ R2 echelle from Milton Roy Co. and slit #4, which has a central width of 511 μ m (or approx. 1.2 arcsec on the sky).

The ESO (La Silla) data were acquired with FEROS (Kaufer et al. 2000), a fiber fed cross-dispersed spectrograph with an R2 79 gr mm⁻¹ echelle grating. The detector was a 2048 \times 4096 EEV CCD with 15 μ m pixels. The FEROS resolving power was about 45 000, which is roughly 20% lower than that of the 2dcoude spectra. This instrument has a fixed configuration, but provides better coverage than the 2dcoude for a single setting: approximately from 350 to 920 nm, leaving two gaps at \sim 853 and 870 nm. Most of the observations from the May and September 2001 runs were obtained in “object-calibration” mode with FEROS: the Th-Ar lamp was on during the stellar observations and its light fed to the spectrograph. This mode was selected due to the fact that the spectra were obtained in between observations for a different program, for which an accurate wavelength calibration was crucial. This turned out to be a disadvantage as, in some cases, scattered light from Ar lines in the red affected the stellar spectra.

Aiming for very high signal-to-noise ratios, at least two exposures per setting were obtained at McDonald. Due to a more limited observing time, a lower *S/N* was reached for the stars observed from ESO, for which a single exposure was typically obtained. About 2/3 of the sample was observed from McDonald. Figure 3 compares the McDonald and ESO spectra of HIP 10798 in the region of the Ca I line at 616.2 nm.

The spectra were reduced with IRAF², using the *imred*, *ccdred*, and *echelle* packages. The processing included overscan subtraction, flatfielding, scattered light removal, optimal extraction and wavelength calibration. Th-Ar observations were very frequent at McDonald. These were combined into an atlas available from the *www*³ (Allende Prieto 2002a). The instrumental response, dominated by the blaze function characteristic of an echelle spectrograph, was carefully removed by two-dimensional modeling following Barklem et al. (2002). The *blue* and *red* setups (McDonald spectra) were combined. Finally, the orders were merged into a continuous spectrum.

In an attempt to produce a highly homogeneous archive, the final spectra were velocity corrected using the central wavelengths of hundreds of solar atomic lines as reference (Allende Prieto & García López 1998). The McDonald spectra were then truncated to the wavelength range 362–1044 nm, while the ESO spectra were restricted to the range 362–921 nm. Errors in the fluxes were estimated from three sources: the Poisson noise ($\sqrt{\text{photons}}$), the continuum placement, and an absolute limit imposed by the best correction of pixel-to-pixel sensitivity variations we can achieve. The uncertainty in the continuum placement for McDonald spectra was estimated by comparing our “sky-light” spectrum, obtained through a port that brings day light from the sky to the slit room, with the solar flux atlas of Kurucz et al. (1984). For the ESO spectra we compared spectra of stars observed both from ESO and McDonald. Figure 4 shows the different error contributions adopted for the McDonald sky (solar) spectrum.

In Fig. 4, the largest differences between the McDonald sky spectrum and the Kurucz et al. (1984) solar atlas (thick solid line) are due to difficulties in selecting uniquely the position of the pseudo-continuum in the blue wavelengths due to severe line absorption, and to the presence of telluric features and different observing conditions in the red and infrared part of the spectrum. The zigzagging shape of the Poissonian limit curve (thin solid line) is caused by the combination of multiple observations of the same spectral segments in contiguous orders of the same setting, and also by the overlapping wavelength coverage between the two settings. The wide peak at \sim 500 nm corresponds to the so-called “picket fence” in the McDonald spectrum – stray light reflected by the CCD back to the grating. It is also worthwhile to mention that the ESO spectra at and near H α have large error bars due to a reflection from the fiber, and thus the H α spectrum in the ESO spectra is unreliable. An error spectrum has been assembled along with each stellar spectrum, which reflects the combined error as discussed above.

The spectra are archived in FITS⁴ format, and are available through the internet at the S⁴N site⁵.

² IRAF is distributed by the National Optical Astronomy Observatories, which are operated by the Association of Universities for Research in Astronomy, Inc., under cooperative agreement with the National Science Foundation.

³ <http://hebe.as.utexas.edu/2dcoude/thar>

⁴ Flexible Image Transport System; see e.g.

<http://fits.gsfc.nasa.gov/>

⁵ <http://hebe.as.utexas.edu/s4n/>,

<http://www.astro.uu.se/~s4n/>

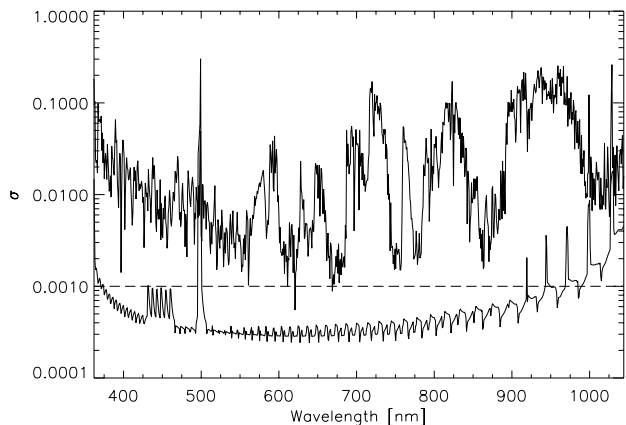


Fig. 4. Contributions to the error in the normalized fluxes for the day light spectrum acquired with the 2dcoudé: continuum placement (thick solid line; derived by direct comparison with the solar flux atlas), Poissonian limit (thin solid), and pixel-to-pixel sensitivity corrections (horizontal dashed line).

3. The S⁴N catalog

3.1. Stellar parameters

The “traditional” procedure to derive stellar parameters for a spectroscopic analysis involves the use of photometry and the spectra themselves. Among the photometric calibrations available to derive the stellar effective temperature, those based on the infrared flux method (IRFM, Blackwell et al. 1977) have been proven very precise and were adopted here – always assuming that the reddening must be negligible within 15 pc. Optical and infrared colors are only weakly sensitive to other stellar parameters. The extreme accuracy of the parallaxes provided by the *Hipparcos* mission for the nearest stars, can be exploited to tightly constrain their brightness and gravity. Such gravities are practically independent from model atmospheres. Our atmospheric stellar parameters are, therefore, independent from the high-resolution spectra, and can be considered fairly robust against the subtleties involved in the interpretation of the high-resolution spectra.

3.1.1. Photometry

Visual magnitudes, $b - y$ and c_1 indices were compiled from Hauck & Mermilliod (1998). Sometimes this source does not provide uncertainties for the data, and we adopted 0.01 mag. When V magnitudes were not available from Hauck & Mermilliod, we searched Kornilov et al. (1991), correcting their values using

$$V = V_K - 0.0019 - 0.061(B - V)_K + 0.072(R - I)_K, \quad (1)$$

where the subscript “K” indicates Kornilov et al. magnitudes, for which we adopted an error of 0.01 mag. This correction follows the recommended transformation by Kornilov et al. (1996). When a star was not in any of these sources, we used H_p from *Hipparcos*, the *Hipparcos* ($B - V$) and the Simbad ($U - B$)⁶ with Harmanec’s (1998) formulae to estimate V ,

⁶ Except for HIP 17420 with no ($U - B$) from Simbad, for which we adopt +0.49 as for a similar star: HIP 84405.

and assign either 0.01 mag of error or the 1σ uncertainty in H_p , whatever is larger. We also compiled $B - V$, $V - I$, H_p , V , and their uncertainties from the *Hipparcos* catalog. These data are available on the S⁴N web site.

3.1.2. Effective temperature

We used the Strömgren photometry and the ($B - V$) index with the Alonso et al. (1996; 1999a) calibrations to derive T_{eff} . The IRFM is based on the comparison between the bolometric flux and the monochromatic flux at a selected wavelength in the infrared. Following the application of the IRFM to derive T_{eff} for a large number of stars, Alonso et al. derived photometric calibrations. Use of such calibrations does not require bolometric fluxes and benefits from the statistical elimination of outliers. Our effective temperatures are based on such photometric calibrations, which are also dependent (although weakly) on the stellar metallicity and surface gravity. We begin by assuming $[\text{Fe}/\text{H}] = 0$ ⁷. Then, other stellar parameters, including $[\text{Fe}/\text{H}]$, are determined from the spectrum (see below), and a second iteration is applied to derive the T_{eff} s in Table 2. The error bars assigned to the temperatures have been derived from propagating the uncertainties in the photometry through Alonso et al.’s polynomials. We found the calibration based on ($b - y$) and c_1 to provide slightly warmer temperatures than the values from ($B - V$) by an average of 42 ± 6 K, with an rms difference of 61 K.

An independent assessment of the scale of effective temperatures can be obtained by exploiting the sensitivity of the wings of Balmer lines to the thermal structure of deep atmospheric layers. Echelle spectrographs are not ideally suited for measuring the shape of broad features such as the wings of Balmer lines, but as we explained in Sect. 2, we paid particular attention to the continuum normalization of our spectra. The $H\alpha$ profiles in the ESO spectra are unreliable, as suggested by the difficulties encountered in the normalization process. However, we deem $H\beta$ for these spectra as “reliable”, and both $H\alpha$ and $H\beta$ in the 2dcoudé spectra, as “highly reliable”. We calculated synthetic profiles for $H\alpha$ and $H\beta$ as described by Barklem et al. (2002). Stark broadening is described by the model-microfield method calculations of Stehlé & Hutcheon (1999) and self-broadening by calculations of Barklem et al. (2000a,b). Radiative broadening is included, and so is an estimate of the helium collisional broadening (based on rescaling of Barklem & O’Mara 1997), although both effects are small. The model atmospheres were computed with the same version of the MARCS code as the models employed to derive abundances (see Sect. 3.3). The only differences affect the convection parameters. Convection is described by the mixing length treatment, where for our purposes the most important parameters are the mixing-length l , which is usually expressed in units of the pressure scale height as the mixing-length parameter $\alpha = l/H_p$, and a second parameter y describing the temperature structure within convective elements (see Henyey et al. 1965 for details). The standard set of parameters in the MARCS

⁷ For an element “El” we define $[\text{El}/\text{H}] = \log\left(\frac{N(\text{El})}{N(\text{H})}\right) - \log\left(\frac{N(\text{El})}{N(\text{H})}\right)_\odot$, where N represents number density.

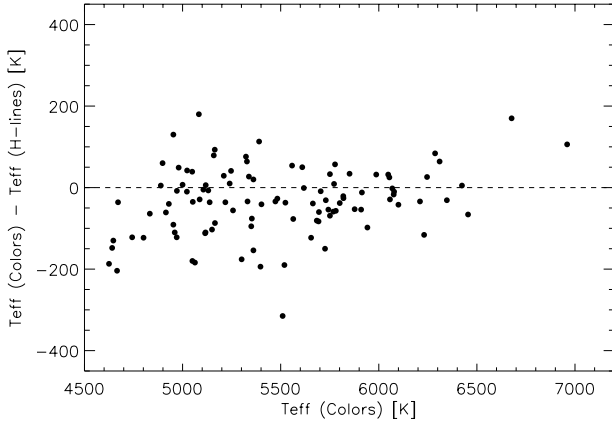


Fig. 5. Differences between the color-based effective temperatures derived from IRFM calibrations and those from fitting the wings of H α and H β .

code are $\alpha = 1.5$ and $y = 3/(4\pi)^2$, and these are adopted for the models used in the abundance analysis. As seen in Barklem et al. (2002; see also Fuhrmann 1998 and references therein), a better match to the observed profiles can be achieved by reducing the mixing length. Thus, for our analysis of hydrogen lines we adopted a model grid with $\alpha = 0.5$ and $y = 0.5$ as in Barklem et al. (2002). We note that the different values have a negligible impact on the overall temperature scale (Barklem et al. 2002). The effective temperatures were determined by χ^2 fitting as described in Barklem et al. (2002).

Figure 5 shows the differences between the IRFM-based T_{eff} s and those from Balmer lines (weighted average of H α and H β). The agreement is satisfying; Balmer lines temperatures are warmer with a mean difference of just 35 ± 15 K, and an rms difference of 84 K. Figure 5 indicates that the Balmer-line temperatures may be slightly higher for stars with $T_{\text{eff}} < 4900$ K⁸. A similar effect was also noted by Barklem et al. (2002) for a different sample, but, as they remarked, the reader should bear in mind that errors in Balmer-line temperatures are largest in that domain due to a) the reduced sensitivity of the line wings, and b) an increasing contamination by metallic lines. The second effect can potentially induce a bias in the observed sense. Balmer-line T_{eff} s might also be slightly cooler for the warmer stars in our sample.

Recently, Kovtyukh et al. (2003) have derived effective temperatures for late-type dwarfs using line-depth ratios. From 13 stars in common, we find their temperatures systematically higher by 119 ± 12 K ($\sigma = 43$ K) in the range $5000 < T_{\text{eff}} < 6000$ K. An aberrant exception takes place for HIP 23311 (HR 1614), for which they derived 4945 K, but our preferred value is 4641 K. We note that Feltzing & Gustafsson (1998) found 4625 K from Strömgren photometry, and Feltzing & Gonzalez (2001) arrived at 4680 K from the excitation

⁸ A particular remark should be made about the T_{eff} for HIP 37826 (Pollux), for which we obtain 4662 ± 75 K from $(b-y)$, and 4684 ± 155 K from $(B-V)$. Although we adopt the weighted average for consistency, both the Balmer profiles and the literature, in particular the direct (rather than based on calibrations of T_{eff} vs. colors) value from Alonso et al. (1999b), show a tendency toward a slightly higher value than from $(B-V)$.

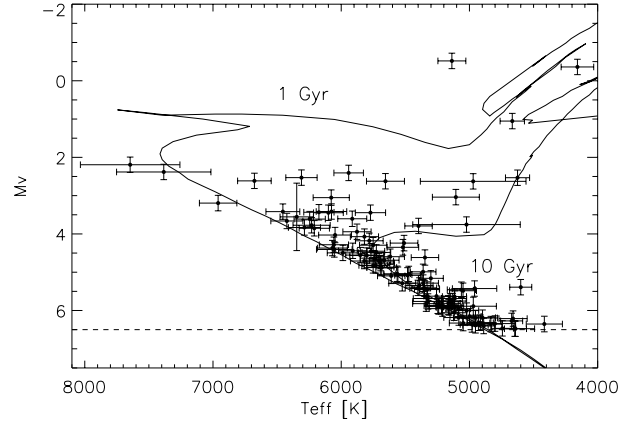


Fig. 6. Distribution of the sample stars in the M_V versus T_{eff} plane.

equilibrium of neutral iron and nickel⁹. From fitting the wings of Balmer lines, we obtain an intermediate value of 4789 ± 110 K.

3.1.3. Metallicity, surface gravity, age, micro and macroturbulence

Metallicities are first estimated from the automated system described by Allende Prieto (2003). Gravities (and ages when possible) are then estimated from T_{eff} , M_V , and $[\text{Fe}/\text{H}]$, by using Bertelli et al. (1994) isochrones in a similar manner to Allende Prieto et al. (2003) and Reddy et al. (2003). More details are provided in Appendix A. A first abundance run with the selected spectral line profiles and using MARCS models (see Sect. 3.3) provided refined values for $[\text{Fe}/\text{H}]$, the microturbulence (ξ), and the macroturbulence (η), that were also used to determine the final T_{eff} (from photometry) and gravities (from the isochrones). The final stellar parameters are listed in Table 2. Figure 6 displays the distribution of the stars in the M_V vs. T_{eff} plane. Two solar-composition isochrones of ages 1 and 10 Gyr are also shown.

The derived values for the microturbulence ($\xi \equiv \sqrt{2}\sigma$, where σ is the standard deviation of a Gaussian distribution) are a function of the T_{eff} and $\log g$ of the stars, as previously found by other authors (e.g. Nissen 1981; Edvardsson et al. 1993; Reddy et al. 2003). For our sample, the expression

$$\begin{aligned} \xi = & 1.645 + 3.854 \times 10^{-4}(T_{\text{eff}} - 6387) \\ & - 0.6400(\log g - 4.373) - 3.427 \times 10^{-4} \\ & \times (T_{\text{eff}} - 6387)(\log g - 4.373) \text{ km s}^{-1} \end{aligned} \quad (2)$$

predicts ξ with an rms scatter of 0.14 km s^{-1} .

3.2. Kinematics

Radial velocities were compiled from the catalogs of Barbier-Brossat & Figon (2000) and Malaroda et al. (2001). Proper motions and parallaxes were extracted from the *Hipparcos* catalog (ESA 1997). We derived stellar UVW galactic velocities following Johnson & Soderblom (1987), but as all

⁹ Note, however, that these authors determined a gravity for this star based on the iron ionization balance which is about 0.6 dex lower than our value (see the discussion in Sect. 4).

Table 2. Stars in the sample.

<i>Hipp.</i> #	T_{eff}	σ	$\log g$	σ	[Fe/H] ^a	ξ	η
	(K)		(<i>cgs</i>)			(km s ⁻¹)	(km s ⁻¹)
<i>Sun</i>	5777	10	4.437	0.001	7.55	1.25	3.27
171	5361	119	4.610	0.040	6.78	1.21	3.01
544	5353	97	4.553	0.047	7.60	1.25	3.75
1599	5851	114	4.468	0.067	7.30	1.28	3.68
2021	5772	118	3.999	0.098	7.43	1.38	4.02
3093	5117	94	4.576	0.040	7.65	0.93	2.94
3765	4980	92	4.652	0.051	7.24	1.17	3.18
3821	5801	132	4.470	0.074	7.24	1.29	3.36
4148	4898	101	4.631	0.042	7.36	1.13	3.21
5336	5323	119	4.665	0.043	6.74	1.34	2.82
7513	6100	116	4.166	0.103	7.60	1.60	6.09
7751	5083	117	4.632	0.049	7.36	1.10	3.20
7918	5768	107	4.422	0.079	7.49	1.22	3.50
7981	5138	93	4.602	0.044	7.45	1.04	2.94
8102	5328	110	4.622	0.054	7.03	1.14	2.82
8362	5257	98	4.576	0.048	7.50	1.06	2.90
10 138	5159	100	4.615	0.048	7.32	1.12	3.23
10 644	5664	115	4.465	0.088	7.06	0.86	3.75
10 798	5338	105	4.632	0.053	7.08	1.12	2.81
12 777	6210	118	4.350	0.066	7.51	1.49	5.60
12 843	6231	145	4.339	0.067	7.59	1.61	13.04
13 402	5087	96	4.598	0.040	7.65	1.33	3.77
14 632	5877	110	4.271	0.099	7.59	1.29	3.78
14 879	6078	141	3.982	0.098	7.32	1.38	4.16
15 330	5610	107	4.552	0.058	7.24	1.23	3.48
15 371	5751	111	4.517	0.063	7.24	1.24	3.48
15 457	5564	104	4.523	0.057	7.49	1.24	3.90
15 510	5390	106	4.578	0.051	7.16	1.17	3.30
16 537	5052	100	4.621	0.044	7.47	1.15	2.97
16 852	5914	113	4.123	0.091	7.44	1.35	3.74
17 378	5023	419	4.145	0.181	7.62	1.04	3.07
17 420	4801	161	4.633	0.047	7.41	1.00	2.79
19 849	5164	98	4.614	0.048	7.34	1.06	2.96
22 263	5695	106	4.504	0.058	7.45	1.25	3.46
22 449	6424	125	4.336	0.060	7.61	1.69	9.92
23 311	4641	86	4.626	0.024	7.81	1.08	2.94
23 693	6069	117	4.451	0.064	7.35	1.46	8.90
24 608	5137	109	2.508	0.117
24 813	5781	108	4.325	0.097	7.57	1.24	3.35
26 779	5150	95	4.584	0.041	7.66	1.08	3.24
27 072	6287	125	4.362	0.064	7.48	1.46	5.78
27 913	5820	108	4.485	0.059	7.44	1.39	5.80
29 271	5473	102	4.507	0.059	7.58	1.01	3.43
32 349
37 279	6677	131	4.081	0.099	7.63	1.72	4.41
37 349	4889	89	4.623	0.038	7.55	1.20	3.03
37 826	4666	95	2.685	0.091
40 693	5331	98	4.569	0.050	7.42	1.13	2.90
41 926	5210	104	4.631	0.057	7.16	1.17	2.94
42 438	5684	116	4.514	0.061	7.36	1.43	5.86
42 808	4930	89	4.619	0.038	7.61	1.19	3.84
43 587	5063	110	4.558	0.038	7.87	0.92	3.33

^a These iron abundances were derived from the simultaneous inversion of all iron lines. These values were adopted for the model atmospheres but are not the same as those used in the discussion to follow in Sect. 5, which are based on Fe I lines only.

Table 2. continued.

<i>Hipp.</i> #	T_{eff}	σ	$\log g$	σ	[Fe/H] ^a	ξ	η
	(K)		(<i>cgs</i>)			(km s ⁻¹)	(km s ⁻¹)
46 853	6310	122	3.913	0.089	7.42	1.71	5.70
47 080	5301	97	4.513	0.061
51 459	6057	114	4.425	0.066	7.42	1.29	3.79
53 721	5751	106	4.349	0.097	7.48	1.18	3.42
56 452	5118	97	4.637	0.054	7.14	1.14	2.76
56 997	5402	99	4.566	0.053	7.42	1.16	3.08
57 443	5558	109	4.545	0.059	7.20	1.12	3.54
57 632
57 757	6076	119	4.142	0.099	7.68	1.49	3.86
58 576	5361	100	4.473	0.076	7.72	1.10	3.24
61 317	5743	109	4.470	0.071	7.26	1.22	3.19
61 941	6960	146	4.304	0.062	7.63	1.91	15.37
64 241	6347	130	4.376	0.149	7.41	1.65	10.72
64 394	5910	111	4.436	0.064	7.54	1.29	3.86
64 797	4915	101	4.632	0.048	7.40	1.10	3.09
64 924	5483	100	4.524	0.058	7.45	1.17	3.01
67 422	4416	141	4.619	0.020
67 927	5942	115	3.750	0.107	7.84	1.72	7.94
68 184	4647	155	4.621	0.027	7.81	0.95	2.97
69 673	4158	127	1.887	0.164
69 972	4671	86	4.620	0.027
71 681	4970	180	4.592	0.038	7.73	0.81	3.32
71 683	5519	123	4.256	0.103	7.67	1.04	3.71
72 659	5350	115	4.576	0.050	7.33	1.19	3.64
72 848	5115	93	4.580	0.040	7.59	1.11	3.66
73 695	5510	108	4.109	0.100	7.12	0.94	3.18
77 257	5819	110	4.297	0.098	7.51	1.33	3.92
77 952	7384	368	4.219	0.066	8.01	2.20	37.72
78 072	6246	122	4.296	0.087	7.40	1.52	6.55
78 775	5247	107	4.646	0.049	6.93	1.17	2.76
79 190	5049	108	4.656	0.058	7.14	1.24	3.28
79 672	5693	108	4.478	0.062	7.53	1.16	3.67
80 337	5730	109	4.499	0.059	7.48	1.33	3.63
80 686	5987	122	4.459	0.061	7.42	1.37	3.92
81 300	5165	93	4.587	0.041	7.56	1.17	3.11
81 693	5655	148	3.672	0.123	7.62	1.38	4.04
84 405	4960	173	4.572	0.037	7.31	1.15	3.37
84 720	5131	106	4.614	0.046	7.15	1.05	3.32
84 862	5618	111	4.405	0.101	7.15	1.25	3.02
85 235	5240	100	4.625	0.052	7.18	1.02	2.86
86 032
86 036	5726	112	4.420	0.082	7.44	1.17	3.93
86 400	4833	86	4.624	0.041	7.50	1.00	3.04
86 974	5397	107	3.965	0.094	7.80	1.04	3.44
88 601	5050	105	4.562	0.038	7.51	0.98	3.13
88 972	5000	91	4.622	0.048	7.39	1.07	2.83
89 937	6048	128	4.336	0.102	7.04	1.02	4.26
90 790	4953	171	4.632	0.047	7.34	1.10	2.90
91 262
91 438	5524	105	4.574	0.055	7.24	1.24	3.40
96 100	5218	96	4.611	0.049	7.33	1.07	2.84
97 649	7646	388	4.230	0.086
97 944	4600	86	4.559	0.032	7.30	2.68	40.82
98 036	5106	183	3.541	0.119	7.36	1.15	3.48
99 240	5347	107	4.248	0.096
99 461	4953	99	4.667	0.054	7.01	1.19	3.17

Table 2. continued.

<i>Hipp.</i> #	T_{eff}	σ	$\log g$	σ	[Fe/H] ^a	ξ	η
	(K)		(cgs)			(km s ⁻¹)	(km s ⁻¹)
99 825	5022	94	4.604	0.044	7.50	1.06	3.21
102 422	4971	412	3.540	0.180	7.41	1.11	3.19
105 858	6054	139	4.474	0.074	6.89	1.27	3.62
107 556	7317	...	4.917
109 176	6455	132	4.298	0.075	7.45	1.53	5.32
110 109	5704	112	4.488	0.072	7.21	1.24	3.44
113 368
114 622	4743	86	4.628	0.035	7.64	1.00	3.01
116 727	4625	94	3.473	0.196
116 771	6174	118	4.181	0.104	7.46	1.39	4.71
117 712	4660	110	4.712	0.040	6.62	0.02	4.35

Hipparcos astrometry is given in the ICRS system J1991.25 (TT), we use $\alpha_{\text{NGP}} = 192.85948$ deg, $\delta_{\text{NGP}} = 27.12825$ deg, and $\theta_0 = 122.93192$ deg (ESA 1997; vol. 1). We modified Johnson & Soderblom’s formulation to account for the correlations among the errors in the astrometric parameters given in the *Hipparcos* catalog. The details are explained in Appendix B. No corrections have been introduced for the solar peculiar motion. The derived galactic velocities and input data are given in the electronic Table 3.

3.3. Chemical abundances

We carried out an extensive search for atomic data, mainly transition probabilities, for elements producing lines in the spectral range of our observations. Our search concentrated on reliable laboratory measurements and accurate theoretical calculations. Candidate lines were examined in the high-dispersion atlases of Arcturus (Hinkle et al. 2001), Procyon (Griffin & Griffin 1979; Allende Prieto et al. 2002a), and the Sun (Kurucz et al. 1984), to identify the best abundance indicators.

A total of 68 features were selected. These features were single-component lines, or the result of multiple transitions (hfs, isotopic shifts, and blends), requiring 275 components and providing abundances for 22 chemical elements. Our analysis considers line profiles and, therefore, we were able to use full profiles or parts of line profiles. Natural and van der Waals broadening were accounted for using data from VALD¹⁰ (Kupka et al. 1999) and the calculations of Barklem et al. (2000c, and references therein) respectively. Hyperfine structure and isotopic splittings were considered for lines of Cu I (Kurucz’s web site¹¹), Sc II (data compiled by Prochaska & McWilliam 2000 for $\lambda 6245.622$ and $\lambda 6604.6$; from Mansour et al. 1989 for $\lambda 6300.684$ and $\lambda 6320.843$), Mn I (compiled by Prochaska & McWilliam 2000), Ba II (compiled by McWilliam 1998) and Eu II (Lawler et al. 2001). Solar isotopic ratios were always assumed. Table 4, available only electronically, provides a summary of our adopted wavelengths, excitation potentials, and transition probabilities.

The parts of the spectrum selected for the analysis define a “mask” that we use for all late-type stars. We exclude the core of strong lines (relative flux lower than 60% of the pseudo-continuum level), in an attempt to minimize the impact of departures from LTE. We analyze the spectra with MISS (Allende Prieto et al. 1998, 2001), adopting theoretical’97 MARCS LTE blanketed model atmospheres (Gustafsson et al. 1975; Asplund et al. 1997), to find the set of abundances, microturbulence, and macroturbulence that best reproduces the observations. We chose to use a Gaussian broadening function (referred to as “macroturbulence” or η) to account for large-scale turbulence (proper macroturbulence), rotational and instrumental broadening. The determination of abundances, micro, and macroturbulence, is accomplished by minimizing the χ^2 between synthetic and observed line profiles, and this can be carried out with all lines simultaneously, or line-by-line. After preliminary all-lines runs to determine the micro and macroturbulence, and the overall metallicity to be adopted in the calculation of the model atmospheres, we used a line-by-line approach to identify outliers and estimate internal uncertainties. Table 5, available only electronically, provides the final adopted abundances for all stars. These abundances are discussed in Sect. 5.3. The stated uncertainties are the standard deviation from different lines (which is set to zero when there is only one line involved).

The median rms scatter we find for the abundance of a given element in a given star is 0.04 dex, but other systematic contributors exist. Departures from LTE and stellar granulation in the real photospheres will bias abundance estimates from individual lines differently. We refer every single abundance estimate from a line to the solar abundance from the same line. Thus, our approach is *strictly differential*. This should reduce systematic errors due to the shortcomings of our modeling, but given the large spread in atmospheric parameters of our stars, will certainly not succeed in removing them completely. Dealing with NLTE and inhomogeneities is very important in some cases, but exceeds the scope of this work. These errors add to the pool of uncontrolled uncertainties together with unrecognized blends, and errors in the continuum normalization. Finally, even for these nearby stars, errors in the atmospheric parameters are a significant, fortunately controlled, source of uncertainty. We have estimated such errors by repeating the calculations with model atmospheres with perturbed atmospheric parameters. As the gravities and metallicities are precisely determined and these parameters only produce minor changes in the abundances compared to variations in the T_{eff} , we have estimated the effect of increasing the T_{eff} s by 3σ and added that information to Table 5.

Adopting Kurucz (1993) non-overshooting model atmospheres instead of MARCS models, we systematically change the temperature and pressure stratification, and then the derived abundances. Although the changes are generally less than 0.1 dex, for some ranges of the atmospheric parameters and some particular elements they can be somewhat larger. This is illustrated in Fig. 7 for a solar-like star (HIP 22263), two late G-type stars with extreme metallicities in our sample (HIP 171 with [Fe/H] $\simeq -0.8$ and HIP 43587 with [Fe/H] $\simeq +0.3$), and an F-type star with solar-like abundances (HIP 37279).

¹⁰ <http://www.astro.univie.ac.at/~vald/>

¹¹ <http://kurucz.harvard.edu>

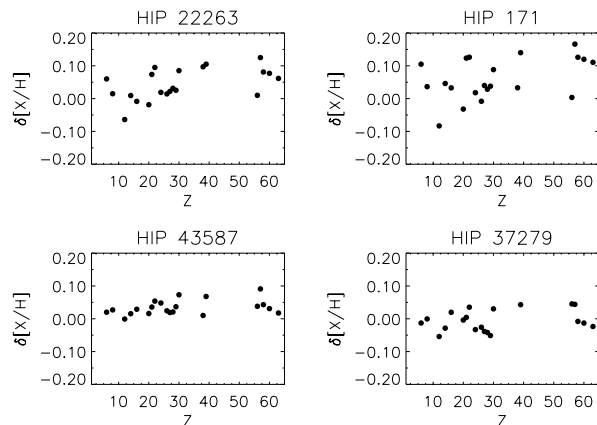


Fig. 7. A sample of the change in the abundances as a function of the atomic number when Kurucz’s (1993) model atmospheres replace MARCS models. A solar-like star (HIP 22263), two late G-type stars with extreme metallicities in our sample (HIP 171 with $[\text{Fe}/\text{H}] \approx -0.8$ and HIP 43587 with $[\text{Fe}/\text{H}] \approx +0.3$), and an F-type star with solar-like abundances (HIP 37279) are shown.

4. Ionization and excitation balance

As a consistency check of the high-dispersion spectroscopic analysis, we examine whether the abundances derived from different lines of the same element agree. Inspection of the abundances from lines of different excitation for Fe I (Ti I, or Ca I) reveals no clear sign of correlations. However, it soon became obvious that iron abundances derived from lines of neutral or ionized iron provided systematically different values. This effect is illustrated in Fig. 8 for Fe and Ca, where it can be seen that the differences can reach ~ 0.5 dex for the most metal-rich stars in the sample. Similar effects are apparent for Si and Ti. A parallel analysis of the nearby star sample based on Kurucz’s model atmospheres shows a similar pattern and magnitude for the ionization imbalance to that found with MARCS models, although the detailed shape of the trends in Fig. 8 changes.

4.1. Precedents

Serious worries about the ionization balance in K-type dwarfs appeared in the work by Oinas (1974). Perrin et al. (1975) revisited the issue and concluded that the magnitude of the problem was overestimated by Oinas and the discrepancies perhaps not significant.

In more recent times, Feltzing & Gustafsson (1998) reported the case of five K-type dwarfs that showed dramatic differences between the abundances from lines of neutral and ionized Fe, and the same effect was apparent for Ca and Cr. Thorén & Feltzing (2000) reanalyzed some of the problematic stars in Feltzing & Gustafsson (1998), suggesting adjustments to the T_{eff} scale to solve the discrepancy.

Very recently, Schuler et al. (2003) have reported similar problems with several K dwarfs in the open cluster M 34. With effective temperatures set to satisfy the excitation equilibrium of Fe I, and gravities assigned from the positions of the stars on the main sequence, their standard LTE analysis resulted in consistent abundances from Fe I and Fe II lines for warm stars

($T_{\text{eff}} \geq 5500$ K), but significant deviations from the ionization balance for most of the cooler dwarfs. Similar to the cases of the nearby K dwarfs and those in the Feltzing & Gustafsson samples, Schuler et al. found significantly larger abundances (up to 0.6 dex) from Fe II lines. The abundances they derived for the K-type stars from Fe I lines were similar to the abundances for warmer cluster stars that did not show the problem. The symptoms are not unique to M 34, as shown by Yong et al. (2004) for the Hyades. The iron abundance inferred from Fe II lines continues to diverge at cooler effective temperatures, exceeding the values from Fe I lines by more than an order of magnitude for stars with $T_{\text{eff}} \sim 4000$ K in this cluster.

As we discuss below, adjusting the stellar parameters to make ends meet is not easily justified for our sample. We should note that most of the previous high-resolution spectroscopic surveys have been for warm (F- and early G) stars with modest iron enrichments (see, e.g. Edvardsson et al. 1993; Reddy et al. 2003). From inspection of Fig. 8 we would expect those studies to find only minor (≤ 0.2 dex) deviations from the LTE ionization balance.

4.2. Errors in the atmospheric parameters?

To reconcile the abundances from neutral and ionized lines for the most metal-rich (and cool) stars in Fig. 8 by modifying the trigonometric gravities would require to decrease them from $\log g \approx 4.6$ to ~ 3.8 . Similarly, the abundances could be reconciled by increasing the T_{eff} by ~ 350 K. Our list of Fe I was punctiliously selected for being clean and having accurate atomic data, but it spans a limited range in excitation energy. A test for HIP 69972 ($T_{\text{eff}} \sim 4700$ K) with 47 Fe I lines drawn from the lists of Blackwell et al. (1995) and Holweger et al. (1995) spanning a range of excitation potential from 0.1 to 4.7 eV shows that a change of 300 K (from 4671 K to 4971 K) results in a change in the slope of the abundances from 0.06 to -0.01 dex/eV, increasing the mean abundance from Fe I by only 0.05 dex, and bringing a marginal improvement in the standard deviation from 0.14 dex to 0.13 dex. The same change is able to bring down the mean abundance derived from Fe II lines by roughly 0.5 dex.

The lines of neutral metals with weak-to-moderate strength in a solar like star tend to become very strong in cool metal-rich stars. With stronger lines the role of the damping constants is enhanced (see, e.g., Ryan 1998). Our analysis makes use of line profiles, rather than equivalent widths, and adopts, when available, the damping parameters calculated by Barklem et al. (see Sect. 3), which we consider reliable to within $\sim 10\%$. Our neutral iron lines are significantly stronger (equivalent widths between 7 and 14 pm) for a star like HIP 69972 than in the Sun. The selected Fe II lines, in turn, are all weaker than 8 pm in the spectrum of HIP 69972. The situation for our calcium lines, however, is quite different, and yet the same shift between the abundances from lines of neutral and ionized species is found. As shown in Fig. 9, even if we only consider the wings of strong Ca lines in the analysis, Ca I and Ca II lines point to quite different abundances. These differences could again be bridged

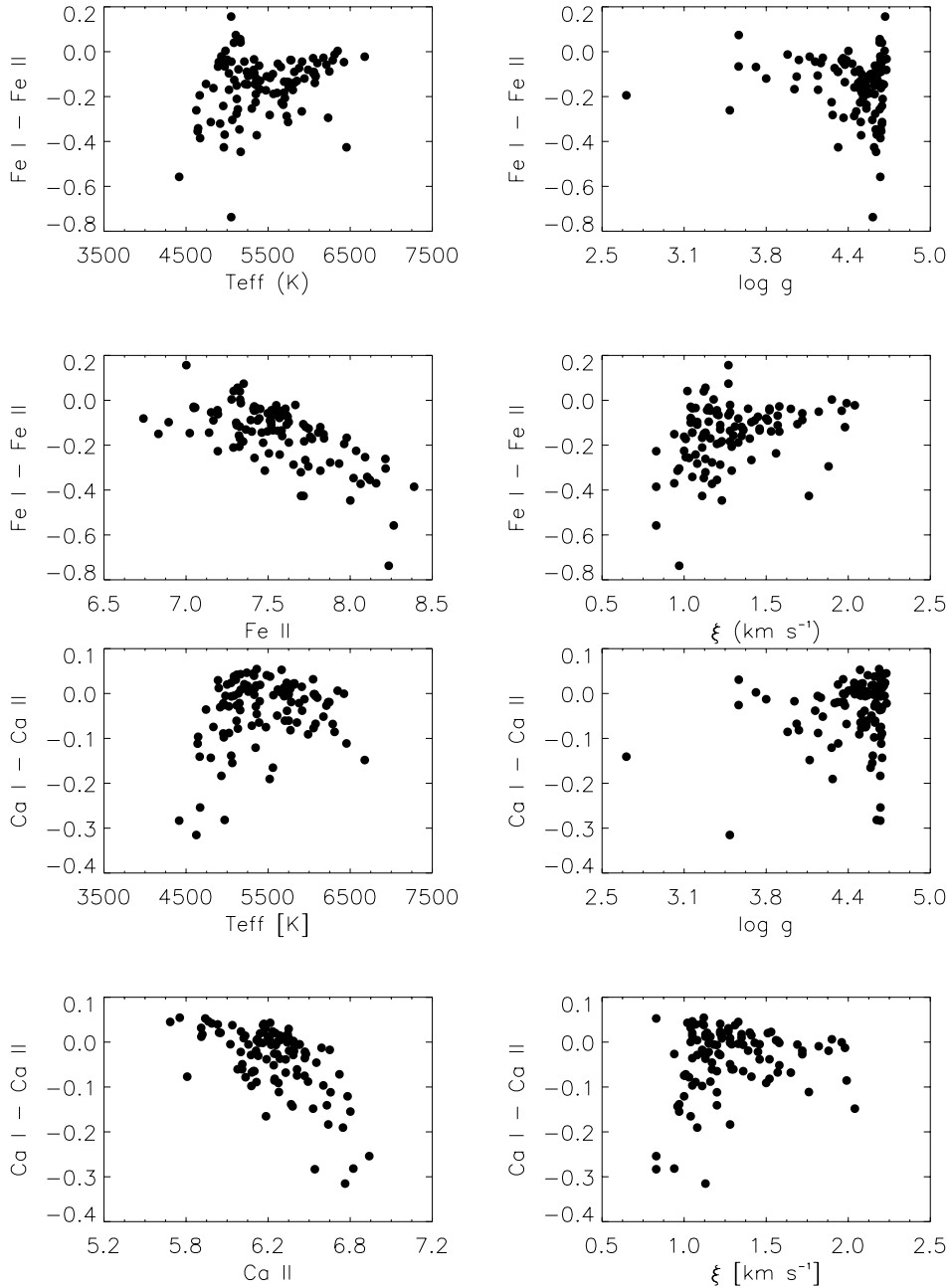


Fig. 8. Differences between the mean iron abundances derived from lines of different ionization stages of Fe and Ca for the stars in the sample as a function of several atmospheric parameters.

by reducing the surface gravity by ~ 0.6 dex, or increasing the effective temperature by ~ 280 K (weakening the Ca I line).

However, a systematic modification by ~ 300 K of the effective temperature from the IRFM calibrations well exceeds the expected uncertainties. For example, the T_{eff} calibration based on $(B - V)$ for dwarfs and subgiants, was derived from data for 410 stars, yielding a standard deviation of 130 K. The calibration for the Strömgren photometry was based on 289 stars with a standard deviation of 141 K. In addition, we find an excellent agreement between the T_{eff} s derived from $(B - V)$ and Strömgren photometry, and, independently, from the analysis of the wings of Balmer lines (see Sect. 3.1). Finally, we should emphasize that the stellar parameters for our sample are well

bracketed by those of the stars used to define the Alonso et al. calibrations.

It is intriguing to consider that the problem may be associated with the trigonometric gravities, but this is extremely unlikely given the size of the discrepancy. From inspection of Table 2, one notices that the corrections required are about 10 times the estimated uncertainties in this parameter. Additionally, Feltzing & Gustafsson arrived at similar gravities for their K dwarfs (in some cases very different from those determined spectroscopically) from trigonometric parallaxes and the pressure-sensitive wings of strong metal lines. Interestingly, comparison between precise stellar radii for stars in eclipsing binaries with evolutionary isochrones has shown that G and

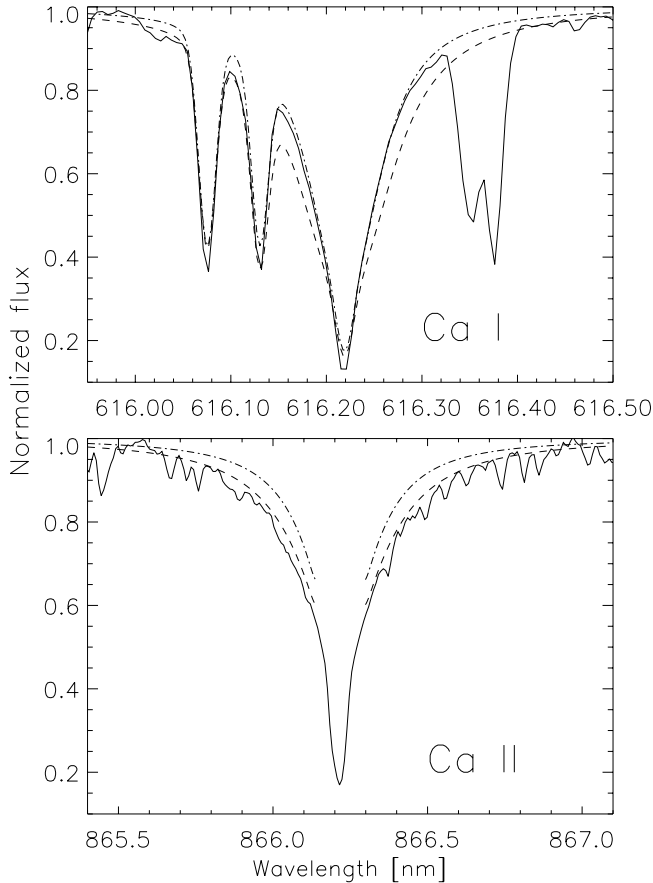


Fig. 9. The Ca I line at 616.22 nm and the Ca II line at 866.22 nm observed in the spectrum of HIP 69972 (solid lines) point to different abundances. The dashed and dash-dotted lines are spectral synthesis for the same appropriate stellar parameters but abundances that differ by 0.25 dex.

K-type stars in detached systems are brighter than predicted (see, e.g., Clausen et al. 1999; Allende Prieto 2001; Torres & Ribas 2002; Ribas 2003). For a reliably determined M_V , predicted radii are smaller by $\sim 10\%$ and therefore gravities larger by ~ 0.1 dex. This effect is as yet not well understood (see, e.g., Lastennet et al. 2003 for a possible solution), but cannot explain the ionization shift we find, because it is too small.

As tempting as it may be to modify the stellar parameters to comply with the ionization balance, we cannot do so without violating robust observational constraints.

4.3. Possible explanations

Ionization shifts with respect to theoretical predictions have been previously reported for metal-poor stars in the form of differences between spectroscopic and trigonometric gravities, and are often attributed to departures from LTE. In fact, deriving higher abundances from Fe II lines seems consistent with the hypothesis of non-LTE overionization as a plausible explanation. The mild correlation of the effect with T_{eff} in Fig. 8 suggests that the most serious discrepancies appear at $T_{\text{eff}} \lesssim 5000$ K, which is where most of the iron becomes neutral in the line formation region, as shown in Fig. 10. Departures from LTE are believed to cause an overionization of iron

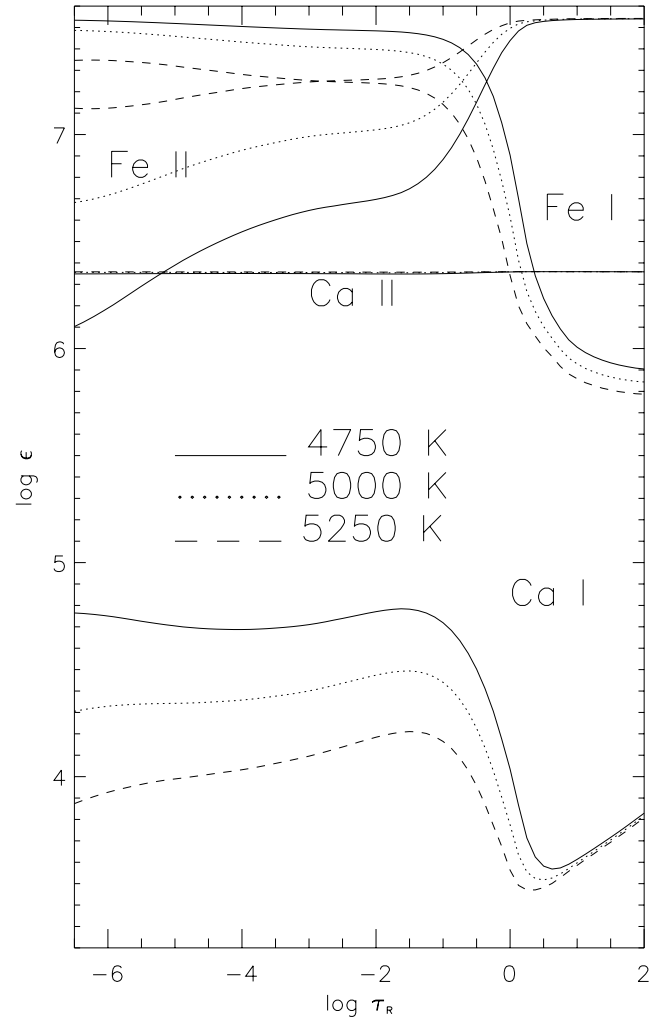


Fig. 10. Logarithm of the ratio between the abundance of neutral or ionized metals and hydrogen atoms for three model atmospheres with $T_{\text{eff}} = 4750$ K (solid line), 5000 K (dotted line), and 5250 K (dashed line). The optical depth scale is based on Rosseland's mean opacity.

compared to LTE predictions in solar-like stars (see, e.g. Shchukina & Trujillo Bueno 2001). The effects are felt in the analysis of Fe I lines, but not for Fe II lines for a solar-temperature dwarf, because most of the iron atoms are ionized in the line-forming region. However, the argument reverses for stars with an effective temperature lower than about 5000 K. Besides, a higher metal abundance in the photosphere decreases gas pressure and enhances electron pressure, shifting the Saha ionization balance towards neutral iron. Thus, departures from LTE in Fe II levels would qualitatively agree with the inconsistencies shown in Fig. 8. However, as shown also in Fig. 10, the situation for Ca I, which is ionized with only 6.1 eV in comparison to 8.9 eV for Fe I, is very different. Ca is still completely ionized everywhere in a solar-composition model atmosphere even for an T_{eff} as low as 3700 K. Yet, calcium shows a similar ionization problem as iron.

Other factors, such as surface inhomogeneities (granulation, spots, etc.), incomplete opacities (due to, e.g., molecules), chromospheric or magnetic activity, may be responsible instead. In an early K dwarf, the region where the largest

velocity and temperature amplitudes of granulation take place is slightly beneath the visible layer (Nordlund & Dravins 1990). As discussed by Dravins & Nordlund (1990a,b) based on 3D hydrodynamical simulations, this results in relatively small line asymmetries and shifts compared to warmer stars, but causes the physical conditions to change very rapidly with the formation height of a line. The formation of high excitation lines may be biased towards the hotter granules, making the lines of ionized species stronger than predicted with a homogeneous model.

In any event, it appears safer in the context of this study to embrace the abundances from the dominant species for the cooler stars (which are also the more metal-rich stars) of our sample. As the abundances from Fe I and II lines are roughly in agreement for most of the warmer stars, in what follows we adopt the mean iron abundance derived from Fe I lines as our metallicity indicator. We still will use line-to-line differential abundances with respect to the Sun, and therefore the notation [Fe/H] will, from now on, refer to Fe I abundances relative to the Sun.

5. Discussion

5.1. Selection of “normal” stars

Some of the observed stars rotate too fast to be handled similarly to the rest of the sample and were not included in the subsequent analysis. These are: HIP 32349, HIP 57632, HIP 77952, HIP 86032, HIP 91262, HIP 97649, HIP 107556, and HIP 113368. HIP 24608 was found to have peculiar profiles and should be studied separately, and HIP 61941 is a visual binary with a separation of about 1.6 arcsec that could not be resolved at the time of the observations. HIP 69673, Arcturus, is the star with the lowest gravity in the sample. Its surface composition does not match that of typical disk stars (Peterson et al. 1993), and was also excluded.

Spectroscopic binaries were not set aside a priori, unless double lines were obvious. The doubled-lined K-type spectroscopic binaries HIP 97944 (HR 7578) and HIP 117712 (HR 9038) will not be discussed here. Both systems were observed when the lines are well separated. HR 7578 has a period of 46.8 days, and an eccentricity of 0.68 (Fekel & Beavers 1983). It is known to exhibit peculiar abundances (Taylor 1970; Oinas 1974). HR 9038 is part of a multiple system, with at least a nearby M 2 component. It has a period of 7.8 days and a circular orbit (Halbwachs et al. 2003), but no abundances have been reported before. The spectra of these systems deserve a more detailed study which would depart from the scope of this paper.

Fast rotators and single-lined binaries are included in the discussion of kinematics. Ignoring the possibility of cleaning our sample with external information will allow us to perform a meaningful comparison with larger samples of more distant, and therefore less-studied, stars (see Sect. 6). Even if the multiplicity fraction is as high as 10–20% (Halbwachs et al. 2003; Mason et al. 2003), this will have only a limited effect on the derived velocity distributions. Fast rotating and double-lined binaries discussed above are excluded from the abundance analysis, but single-lined spectroscopic binaries with

apparently clean spectra are not, as no significant differences were noted between those identified as members of binary systems in SIMBAD and the rest (see below).

5.2. Kinematics and metallicity distribution

In Fig. 11 we show histograms of the galactic velocity components and iron abundances for the sample. Gaussian distributions have been fit to the data, and are usually fair approximations. The zero points of the velocity components reflect the solar motion with respect to its nearest neighbors (what has been sometimes termed the solar *basic* motion). These numbers are in good agreement with older determinations (see, e.g. Delhaye 1965; Woolley 1965) and for U and W , but not for V due to the dependence of this parameter on the stellar population (asymmetric drift), they also agree very well with the solar peculiar motion with respect to the local standard of rest (circular motion; see Dehnen & Binney 1998). The widths of the distributions are consistent with values derived from larger samples, but we will revisit this issue in Sect. 6. To explore the effect of biases due to evolutionary effects (more massive stars that have already died), we have restricted the sample to stars with T_{eff} cooler than 5500 K. Such distributions (dashed lines) have been rescaled to match the maxima of the total distributions and help the eye in the comparison. No significant differences are apparent in the velocities.

The metallicity distribution of nearby late-type stars has been extensively discussed in the literature. This is the first time, however, that it has been derived for an absolute magnitude-limited sample using spectroscopy. A Gaussian provides a fair approximation to the [Fe/H] distribution of our sample. While the width of the distribution is in good agreement with most previous results, the center of the Gaussian, at -0.11 dex, is slightly higher than most studies (but see Haywood 2001, 2002). Restricting the analysis to the coolest stars ($T_{\text{eff}} < 5500$ K), the resulting metallicity distribution is shifted to higher values. Further reduction of the maximum T_{eff} to ~ 5000 K does not alter the [Fe/H] distribution appreciably. The discussion on the ionization balance in Sect. 4 may leave some readers worried about how uncertainties in theoretical model atmospheres might affect the derived distribution. It suffices to say that adopting the average (Fe I + Fe II) abundances, would shift the center of the (full sample – solid line) [Fe/H] distribution in the figure to -0.06 dex.

The existence of super-solar metallicity stars in the local disk has been known for a long time (e.g. Spinrad 1966; Spinrad & Taylor 1969; Taylor 1970). Curiously, the most metal-rich stars are mainly dwarfs and subgiants with spectral types F or later (e.g. Feltzing et al. 2001; Allende Prieto 2002b; Taylor 2002). Figure 12 shows clearly that the most metal-rich stars in our volume-limited sample are also the coolest. Metal-poor main-sequence stars are less luminous than their metal-rich counterparts, and in Fig. 12, the lack of metal-poor stars at the lowest temperatures is, at least in part, the result of having a M_V -limited sample.

HIP 69972 (HD 125072) appears to be the most metal-rich star in the sample. The Fe I-based metallicity is roughly

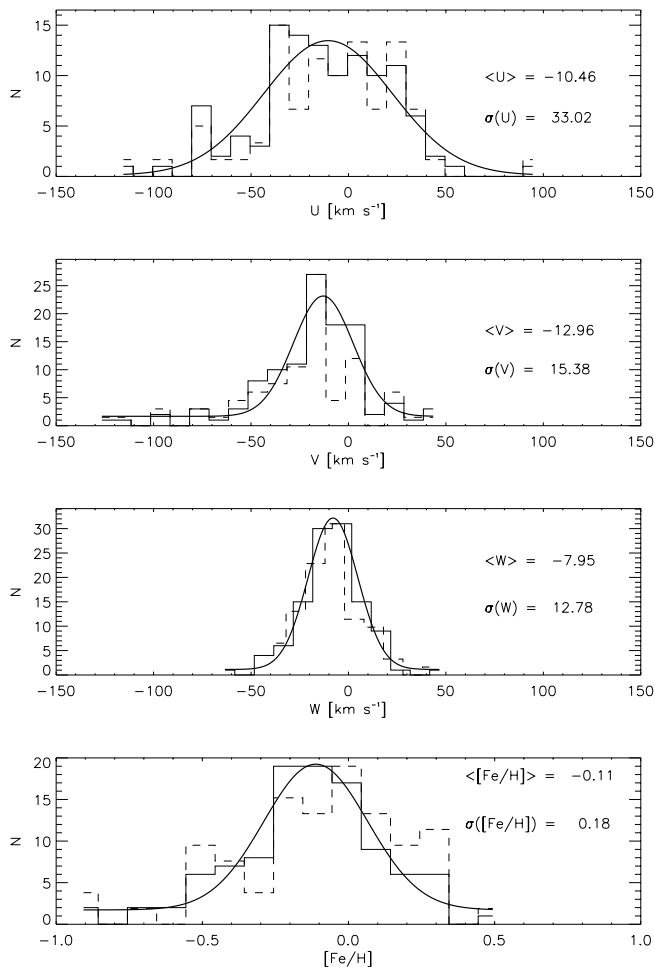


Fig. 11. Histograms of the galactic velocity components (UVW) and the metallicity of the sample stars. The distributions for the complete sample are shown with solid lines. Gaussian curves have been fitted to these distributions and are also shown with continuous solid lines. The dashed-lines show the distributions for the stars with T_{eff} cooler than 5500 K, which have been re-scaled to match the maxima of the all-stars distributions.

+0.5 dex, among the largest values reported in the literature (e.g. Buzzoni et al 2001; Taylor 2002; Chen et al. 2003). The Fe II-based metallicity of this star is about one dex higher than solar but, given the inconsistency between Fe I and Fe II abundances, and the much higher sensitivity of the Fe II lines to temperature changes, we think such a higher abundance is unlikely. This star was previously analyzed by Perrin, Cayrel de Strobel & Dennefeld (1988), who derived a lower value of $[\text{Fe}/\text{H}] = +0.26$ dex¹². Reinforcing the discrepancy, their adopted effective temperature was nearly 300 K warmer than our IRFM value. At least part of the difference can be attributed to their Fe I equivalent widths, which we found, on average, to be $\sim 30\%$ smaller than those we measure in the modern CCD spectrum. Such a large discrepancy is unexpected, given that the reticon spectrum of Perrin et al. had a S/N of 60, and a resolving power similar to ours. Variability could be a

¹² Their differential analysis used sunlight spectra obtained with the same instrument as the stellar spectra. Therefore, the quoted abundance is independent of the adopted iron solar abundance.

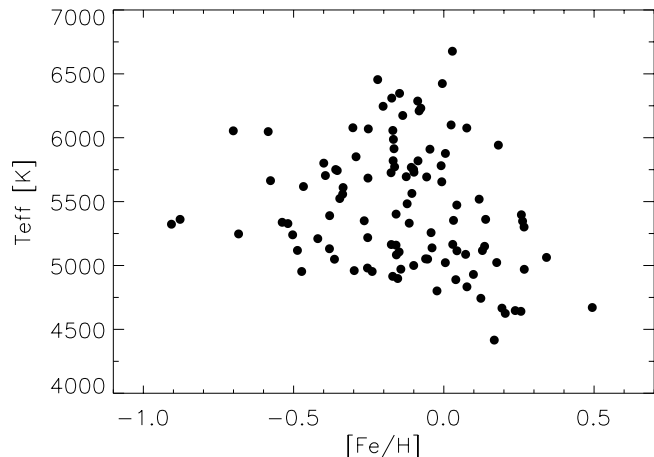


Fig. 12. Fe I metallicities and effective temperatures for the stars in our sample.

possible explanation, but the *Hipparcos* epoch photometry of the star shows a negligible broad-band variability of just 0.015 mag over 2.5 years.

Interesting correlations between abundances and kinematics are apparent in Fig. 13. The velocity components of the stars show the smallest scatter at high iron abundances. The figure for the V component shows an unusually low density of stars with low metallicity and solar-like galactic rotation: the most metal-poor stars either lag or lead the typical thin-disk rotation velocity, with no half measures, but this may be a selection effect introduced by poor statistics. The lower-right panel in the figure shows the age metallicity relation for the stars whose age could be estimated with an uncertainty of 0.7 dex or less. Ages could only be determined for the few stars visibly evolved from the main sequence, but this is still quite informative. This panel warns against interpreting $[\text{Fe}/\text{H}]$ as a clock.

Although the most metal-poor stars are also among the oldest (>10 Gyr), they share ages with some of the most metal-rich stars in the sample, which show thin-disk kinematics. Metal-rich subgiants with old ages have been known for a long time (see, e.g. Schwarzschild 1958; Eggen 1960) and have been confirmed in post-*Hipparcos* studies of the local disk (e.g. Feltzing & Holmberg 2000; Feltzing et al. 2001). Recently, Sandage et al. (2003) have found that evolutionary tracks with a metallicity of $\sim +0.37$ and an age of ~ 8 Gyr were needed to reproduce the reddest subgiants in a *Hipparcos* color-magnitude diagram. Chen et al. (2003) report on spectroscopy of several metal-rich stars with ages >10 Gyr. We estimate, for example, an age of ~ 13 Gyr and a metallicity of $+0.3$ for HIP 99240. Some of the coolest stars in our sample appear to be slightly off the main sequence, and they are most likely binaries. The most notable case is HIP 97944, a BY Dra variable clearly noticeable in Fig. 6.

5.3. Metal abundance ratios

The abundance ratios between iron and other metals have been shown to correlate with the iron abundance for many elements. Such correlations provide a rich database to confront with

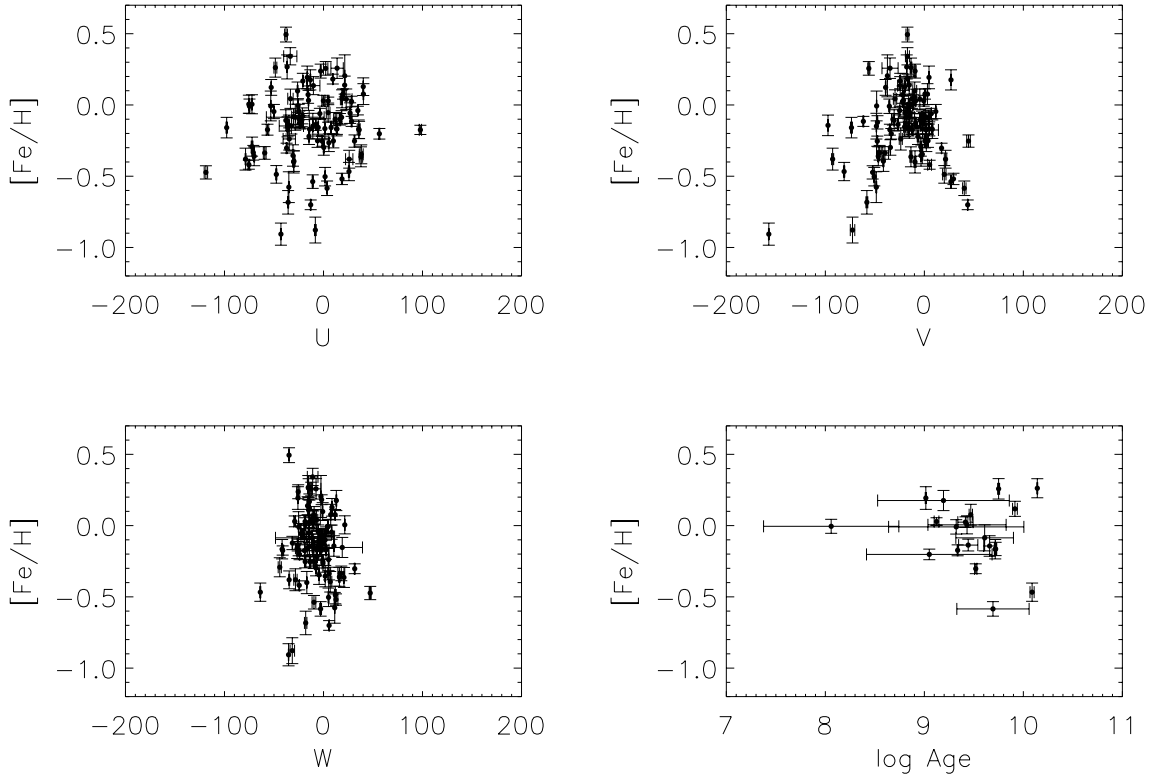


Fig. 13. Distribution of the sample stars in the planes of galactic velocities (UVW) and $[Fe/H]$, and in the plane of age vs. $[Fe/H]$. In the lower-right panel, only stars with relatively small errors in age ($\sigma \leq 0.7$ dex) are shown. The data point with a particularly slow galactic rotational velocity V corresponds to HIP 5336 (HR 321; μ Cas), a well-known metal-poor spectroscopic binary (see, e.g., Haywood et al. 1992). One of the radial velocities in the Malaroda et al. catalog for this star is very different from the other two available measurements, which is surprising given the small semi-amplitude of the primary (the secondary is ~ 6.5 mag fainter). We adopted a recent and very precise determination of the systemic velocity ($V_R = -97.44 \pm 0.07$ km s⁻¹; T. Forveille, private communication) which is in good agreement with the other two measurements in the catalogs.

models of chemical evolution and nucleosynthesis predictions. Because the derived trends may be highly sensitive to modeling errors (see Sect. 4), we have chosen to restrict our study to elements represented in the spectrum with low excitation lines from majority species. Such lines are only weakly sensitive to changes in the adopted model atmosphere and stellar parameters. With this filtering, we limit significantly the number of chemical elements to explore, but we feel that given the apparent inconsistencies discussed earlier, this is the only feasible strategy to obtain meaningful results. Figures 14–16 show the ratios of 16 elements to iron in our sample. Stars with a galactic rotational velocity $V < -62$ km s⁻¹ (or < -50 km s⁻¹ relative to the local standard of rest) are shown in red; all others in blue. Stars labeled in SIMBAD as spectroscopic binaries are also identified with open circles.

Carbon is represented in our analysis by the forbidden line at 8727 Å. This feature is affected by neighbor lines, but we believe they can be properly accounted for at solar T_{eff} s (Gustafsson et al. 1999; Allende Prieto et al. 2002b). A straight least-squares linear fit to the data in Fig. 14 (top left panel) suggests a slope of -0.4 ± 0.1 dex/dex, significantly steeper than the results of Gustafsson et al. (1999) for a sample of disk stars spanning a similar range in metallicity. Our C/Fe ratios exhibit more scatter, most likely due to the larger range in stellar parameters of our nearby stars. Given the weakness and location

of the forbidden line in a crowded region, further analysis will benefit from a higher resolving power to clarify this issue.

Oxygen is represented very sparsely in stellar spectra. The only features we use to derive abundances and discuss here are the [O I] line at 630 nm, and the high excitation IR triplet at 770 nm. While the forbidden line has been shown to be nearly immune to departures from LTE, it is weak and blended with a Ni I line (Allende Prieto et al. 2001; Asplund et al. 2004). The near-infrared triplet lines are an extreme example of departures from LTE, but are stronger and clean for measuring in solar-like and metal-poor stars. The high excitation of the triplet lines also argues against their use for our study, given the problems with the ionization balance (see Sect. 4). In fact, despite our rigorously differential analysis, we notice that an analysis of the triplet lines for stars with atmospheric parameters close to solar, suggests that the Sun is oxygen poor by ~ 0.2 dex.

Some insight can be obtained from a comparison between the triplet-based and [O I]-based [O/Fe] for a solar-like star such as HIP 7918. We have derived an T_{eff} of 5768 ± 107 K, a $\log g$ of 4.422 ± 0.079 , and a metallicity of $[Fe/H] = -0.11 \pm 0.07$. The micro and macroturbulence, as well as the projected rotational velocity are also close to solar. Yet, analysis of the [O I]- Ni I blend leads to an abundance $[O/H] = 0.04$, while analysis of the infrared triplet leads to $[O/H] = 0.20$. If departures from LTE in the triplet lines are

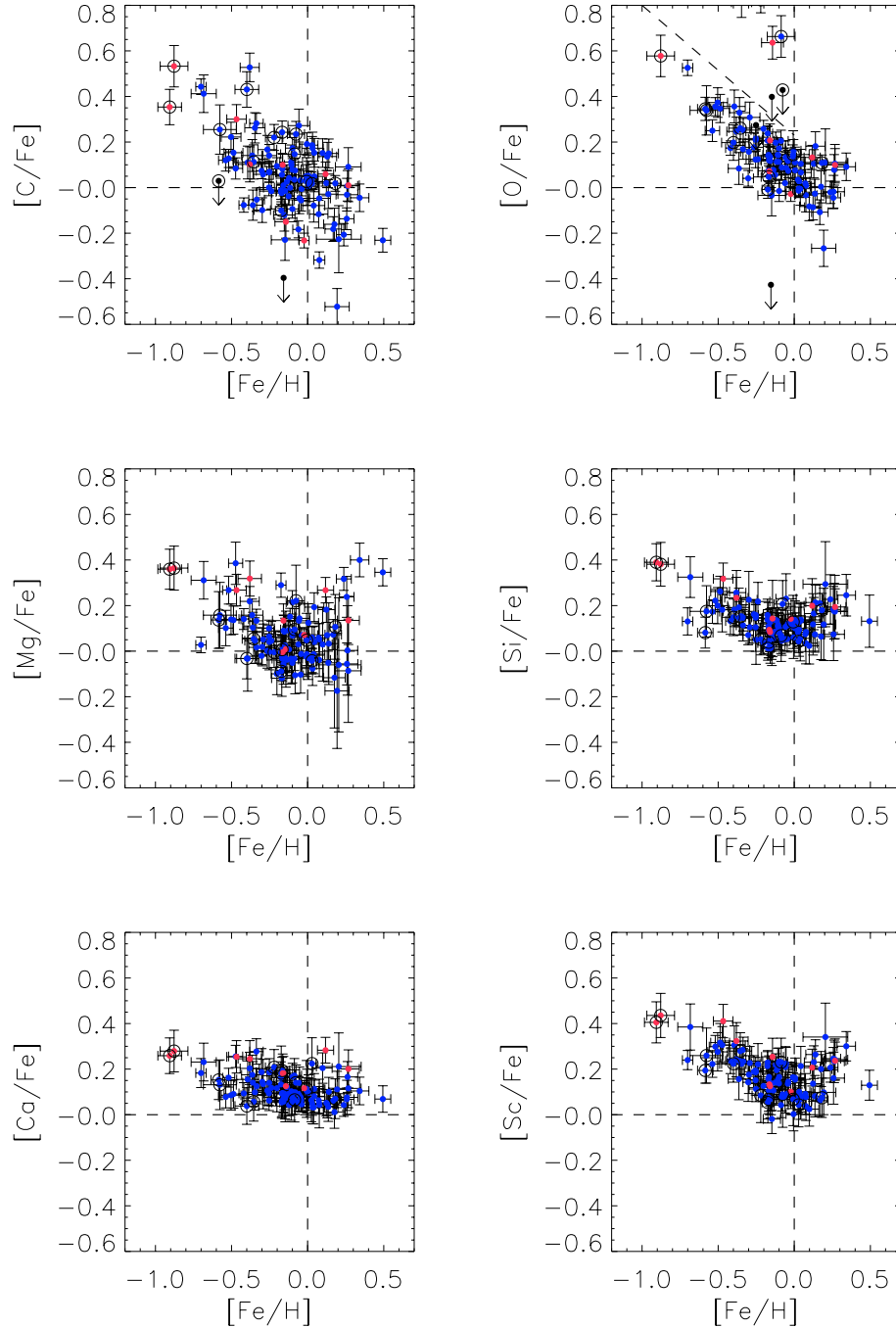


Fig. 14. Abundance ratios between different elements and iron as a function of the iron abundance. Stars with a galactic rotational velocity $V < -62 \text{ km s}^{-1}$ (or $< -50 \text{ km s}^{-1}$ relative to the local standard of rest) are shown in red; all others in blue. Stars labeled in SIMBAD as spectroscopic binaries are identified with open circles.

responsible for this discrepancy, they must depend on parameters other than those considered in a standard analysis (age is a candidate; see Sect. 6). An alternative explanation could be related to the fact that we cannot derive the solar parameters in the same fashion as those for the other stars. The trend of O/Fe in Fig. 14 has been defined from the analysis of the forbidden line. We have accounted for the Ni I blending transition using the Ni abundances determined for each individual star from isolated Ni lines (see below). Some stars artificially show very high values due to blending with telluric lines (above

the dashed line). HIP 109176 is an exception, but it is a spectroscopic binary and our spectra show signs of a second star. HIP 4148 shows an unusually low upper limit, but the [O I]-Ni I blend appears affected by emission. The rest of the stars appear aligned in a pattern very similar to that found by Nissen et al. (2002) for $-0.7 < [\text{Fe}/\text{H}] < +0.25$, with a slope of ≈ -0.5 below $[\text{Fe}/\text{H}] \sim 0$ that flattens out at super-solar metallicities.

The **magnesium** abundance is derived from the Mg I lines at 473.0, 631.9 and 880.6 nm. The strongest line at 880.6 gives a lower abundance than the other two by 0.2–0.4 dex, but it

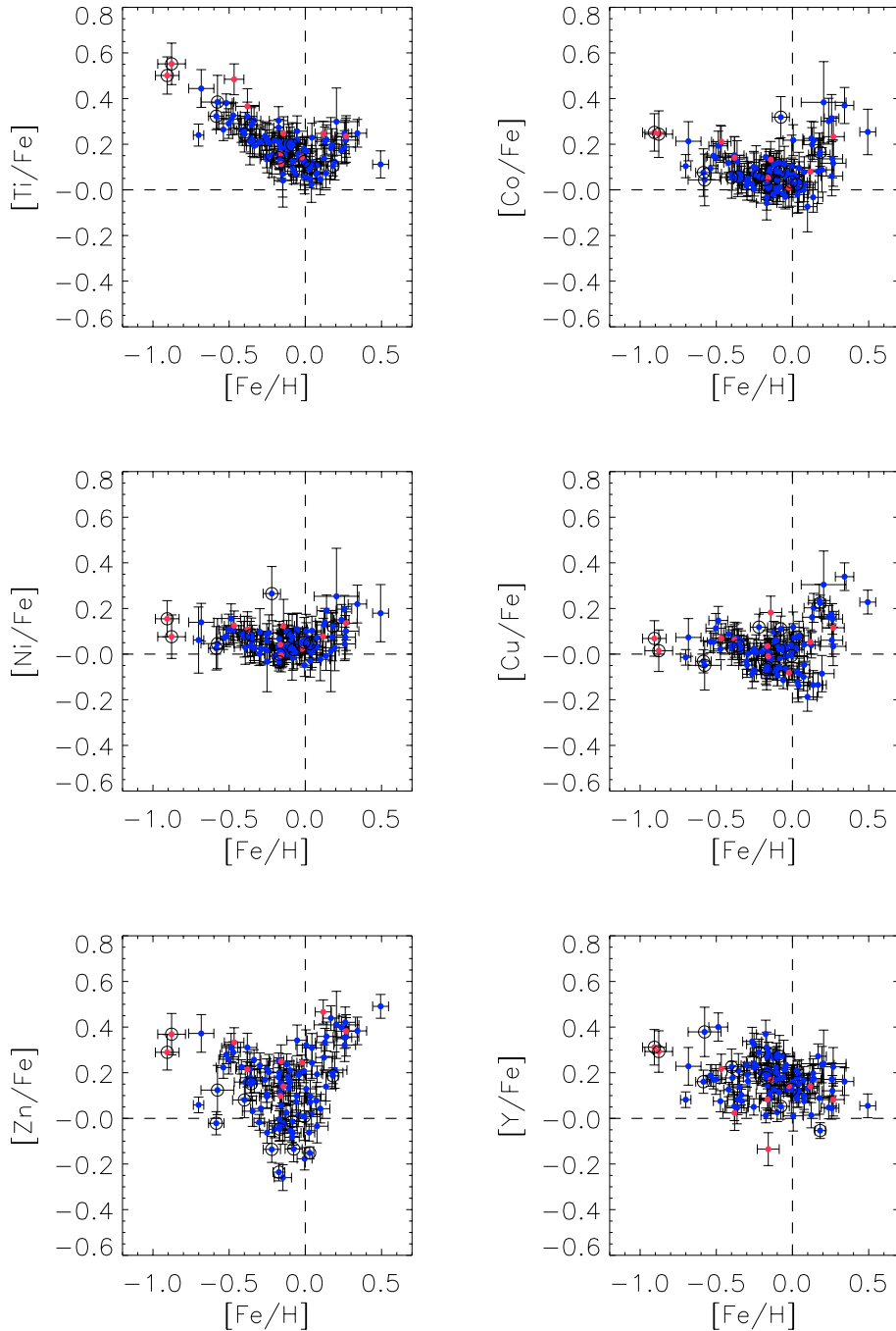


Fig. 15. As in Fig. 14 for other elements.

is unclear which is to be preferred. Our differential analysis, however, largely suppresses such systematic differences. This element shows a pattern similar to other alpha elements, but with somewhat more “noise”. The alpha elements Si and Ti show similar trends. Sc mimics their behavior (compare in particular with Ti). The differences in the abundances of these elements among stars at a given $[\text{Fe}/\text{H}]$ are very likely real, as they appear the same in the three panels. Silicon is measured through numerous lines of neutral Si that show quite consistent abundances for solar and metal-poor stars, but their behavior degrades slightly for $[\text{Fe}/\text{H}] > 0$, even after the abundances derived from two lines in our list that are likely afflicted by

blends are rejected. The abundances from different Sc and Ti lines, however, are internally consistent in our full range of $[\text{Fe}/\text{H}]$. As these two elements are fully ionized in the entire temperature range of our stars, and we use ionized lines, the derived abundances are extremely robust to errors in the stellar parameters.

For metal-poor stars, the ratio of Si, Ti, or Sc to iron grows steadily from solar reaching $\sim 0.4 - 0.5$ dex at $[\text{Fe}/\text{H}] \sim -1$, suggesting a slope between -0.3 and -0.4 dex per dex – significantly steeper than in some of the previous studies. At super-solar metallicities, the trend reverses. This feature contrasts with other analyses, which found such ratios approximately

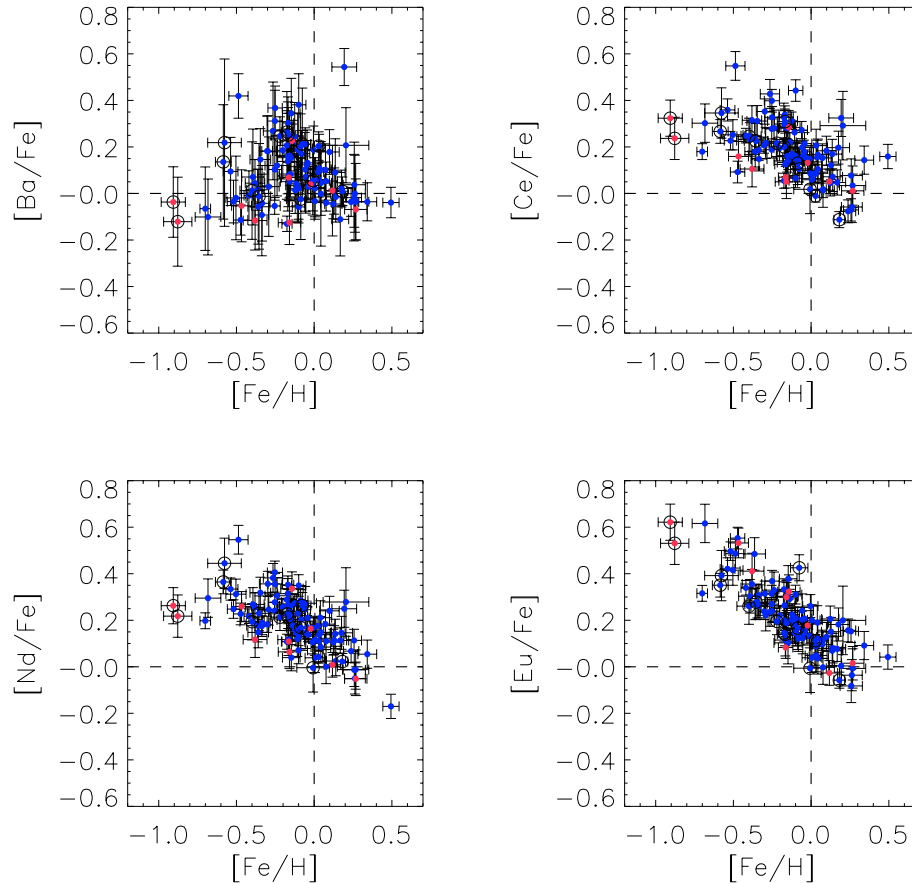


Fig. 16. As in Figs. 14 and 15 for other elements.

flat in metal-rich disk stars (e.g. Bodaghee et al. 2003; Feltzing et al. 2003; Chen et al. 2003; but see Feltzing & Gonzalez 2001, who reported an average $[\text{Si}/\text{Fe}] = +0.12$ for seven metal-rich stars and $[\text{Ti}/\text{Fe}]$ as high as $+0.38$ for HD 32147).

The stars with a galactic rotational velocity less than about -62 km s^{-1} (or -50 km s^{-1} relative to the local standard of rest), shown in red in Figs. 14–16, tend to have abundance ratios near the upper envelope in the trends observed for Mg, Si, Ca, Sc, Ti, Co, Cu, Zn, and Eu, in agreement with previous analyses (e.g., Reddy et al. 2003; Feltzing et al. 2003) but close to the lower envelope for Ba, Ce, and probably Nd.

Calcium was studied with the wings of the strong Ca II lines at 849.8 and 866.2 nm, obtaining fairly similar abundances from both features. The final abundances, however, were derived only from the 866.2 nm line, as this was less contaminated by blending features in the most metallic spectra. This element’s ratio to iron appears flattened compared to Si, Sc or Ti. **Nickel** shows a remarkably flat ratio to iron for metal-poor stars, in agreement with the results from F-type stars (e.g. Reddy et al. 2003). The pattern, however, changes abruptly for the most metal-rich stars. At the coolest temperatures for our stars, a variation of $\sim 300 \text{ K}$ can alter the abundances of our two Ni I lines by 0.05 dex, although in opposite senses due to their different excitation energy. Ni has an ionization potential of 7.64 eV, which is close to the 7.90 eV for iron. The small difference in energy might be enough to introduce significant systematic differences in the variation of their ionization

balances, and therefore little weight should be given to the high abundances found for the most metal-rich (and also the coolest) stars in our sample. **Cobalt**, however, is ionized with 7.88 eV, and therefore the ratio Co/Fe derived from our list of Fe I and Co I transitions should be a somewhat more robust quantity. This is particularly true for the coolest stars in the sample, for which Co I and Fe I are the dominant species. We observe that $[\text{Co}/\text{Fe}]$ increases for lower $[\text{Fe}/\text{H}]$ values, but the most metal-rich stars show even large enrichments in cobalt.

Copper is studied with the Cu I lines at 510.55, 521.82 and 578.2 nm. The abundances they provide are in fairly good agreement for solar-like metallicities and more metal-poor stars, but progressively diverge for higher metallicities¹³. The flat trend with increased dispersion close to solar metallicity is not new (see e.g. Reddy et al. 2003), but the enrichment for metal-rich stars has not been reported before. We have only used the line at 578.21 nm, which gives lower abundances than other transitions in the most metal-rich stars. This feature, again, is insensitive to large corrections in T_{eff} . Nevertheless, it would be very useful to carry out a more detailed study checking for possible blends in the high-metallicity regime. If real, the large enhancement in Cu/Fe is opposite to the values found

¹³ The analysis of the line profiles in the sky spectrum with a MARCS model leads to $\log \epsilon(\text{Cu}) = 4.18$ dex, in good agreement with the value proposed by Grevesse & Sauval (1998) of 4.21, but slightly higher than derived by Cunha et al. (2002) and Simmerer et al. (2003) (4.06 dex).

in very metal-poor halo stars in the field or clusters (Mishenina et al. 2002; Simmerer et al. 2003).

We analyzed the Zn I transitions at 472.22 and 481.05 nm, which provide similar abundances for metal-poor stars, but growing discrepancies at larger metallicities. We noticed that the line at 472.22 nm has significant damping wings, which are systematically underestimated by the Unsöld approximation (adopted lacking better data), leading to higher abundances for metal-rich stars. Thus, we decided to adopt the abundance derived exclusively from the line centered at 481.05 nm. **Zinc** appears more abundant than iron in metal-poor stars than at solar metallicity, and even more enhanced in super-solar metallicity stars.

Yttrium shows a ratio to iron roughly flat, perhaps with a slightly negative slope. The **Ba** abundances, as derived from the resonance line at 455.4 nm and the high-excitation transition at 585.4 nm, show significant scatter, in agreement with previous results (Reddy et al. 2003). The other neutron-capture elements in Fig. 16, **Ce**, **Nd**, and **Eu**, show less scatter as their s-process contribution decreases, although caution should be exercised, as the abundances of some of these elements are derived from a single feature.

Despite the scatter, our **Eu** abundances indicate a decrease in the ratio Eu/Fe with metallicity just slightly faster (a slope of -0.5) than proposed by Woolf et al. (1995; slope ≈ -0.4) or Koch & Edvardsson (2002; slope ≈ -0.3), and especially Reddy et al. (2003; slope ~ 0). The differences with Woolf et al. and Koch & Edvardsson could be related to the Fe scale, which in their case was set by Fe II lines (the dominant species for the temperatures of their stars), or to sampling of different populations within the disk. In our favor we should stress that our analysis of this element benefits from the recent laboratory study of Eu II by Lawler et al. (2001) not available to most authors above. A satisfying agreement (within 0.15 dex) between the abundances that we derive from the resonance line at 412.97 nm and the excited line at 664.51 nm supports our confidence in the new values. We have only used the abundances from the redder feature, which is weaker but we believe cleaner. Koch & Edvardsson (2002) also found a non-zero Eu/Fe ratio at solar metallicity ($[\text{Eu}/\text{Fe}] = +0.04$), albeit lower than ours ($[\text{Eu}/\text{Fe}] = +0.15$).

6. Representativity of the sample

In this study we offer for the first time a census of nearby stars limited in absolute magnitude and distance. Nonetheless, by limiting the distance to only 14.5 pc we are sampling a volume so small that peculiarities of some stars could be erroneously interpreted as representative of the thin disk. Due to *Hipparcos*' completeness limits, expanding significantly the volume for a complete sample requires restricting the analysis to earlier spectral types. We can, however, compose extended samples for which some properties are readily available and explore whether some of the characteristics derived from the S⁴N stars are more generally shared by stars in the local thin disk. Unfortunately, at this time an expanded sample requires use of different, incomplete, catalogs, inevitably introducing new and

complex selection effects. Keeping this in mind, we proceed to carry out such an exercise.

6.1. Kinematics, metallicity, and age for an extended sample

We collected a sample of stars whose astrometric positions, proper motions, and parallaxes were included in the *Hipparcos* catalog and whose radial velocities were part of the *Hipparcos* input catalog, or those compiled by Barbier-Brossat & Figon (2000) and Malaroda et al. (2001). Using a 0.05 degree window to match stars in the *Hipparcos* catalog with the Barbier-Brossat & Figon radial velocity catalog we identify 23 742 stars in common. We found 9312 stars in common between *Hipparcos* and the Malaroda et al. catalog, which concentrates on fainter stars than Barbier-Brossat & Figon's. With a smaller 0.01 deg window we uniquely match 19 072 stars with radial velocities in the *Hipparcos* input catalog with their counterparts in *Hipparcos*. A total of 28 416 stars were in one or more of the radial velocity catalogs and *Hipparcos*. We searched for metallicities ($[\text{Fe}/\text{H}]$) for the sample stars in the catalog of Cayrel de Strobel et al. (2001). This catalog includes metallicities collected from the literature based on one or more sources for 2427 field stars and 582 stars in clusters and associations. Our "extended" sample of stars with metallicities, astrometry, and radial velocities includes 2144 objects.

If we restrict the analysis to the region with $V > -40 \text{ km s}^{-1}$ and $-80 < W < +50 \text{ km s}^{-1}$, contamination by the thick disk and halo should be negligible. Figure 17 reveals that the distribution of stellar velocities can be reasonably well modeled by Gaussians in each direction. Kinematically, these stars belong to the same population as those in the S⁴N sample. The slight differences in the widths for each velocity component can be easily explained by the statistical errors in the smaller sample and the different distribution of spectral types (this affects mostly V ; both samples are dominated by late-type stars, but with somewhat different proportions). The zero offsets – the solar peculiar motion with respect to its neighbors – derived from the extended sample agree with those determined from the S⁴N stars within 1 km s^{-1} . Some spikes in the velocity distributions shown in Fig. 17 are statistically significant. These are well-known real structures in the solar neighborhood. Although the observed star counts are modeled here as a single Gaussian distribution, the velocity structure of the solar neighborhood is quite complex. Chereul et al. (1999) have studied the positions and kinematics of A-F *Hipparcos* stars within 125 pc from the Sun, identifying several well-known groups as well as some new clusters, associations and moving groups. For example, in a plot of W vs. U or V vs. U , the Hyades cluster can be immediately recognized as a clump centered at $(U, V, W) \approx (-43, -18, -2) \text{ km s}^{-1}$, which is clearly visible in the panel for V in Fig. 17. Far from being in perfectly circular orbits, the thin disk stars in the solar neighborhood – and likely elsewhere – show a rich structure in phase space (see, e.g., Eggen 1998).

Figure 17 also shows the metallicity distribution for thin disk stars. It is centered at $[\text{Fe}/\text{H}] = -0.09$ and has a $1\text{-}\sigma$ width

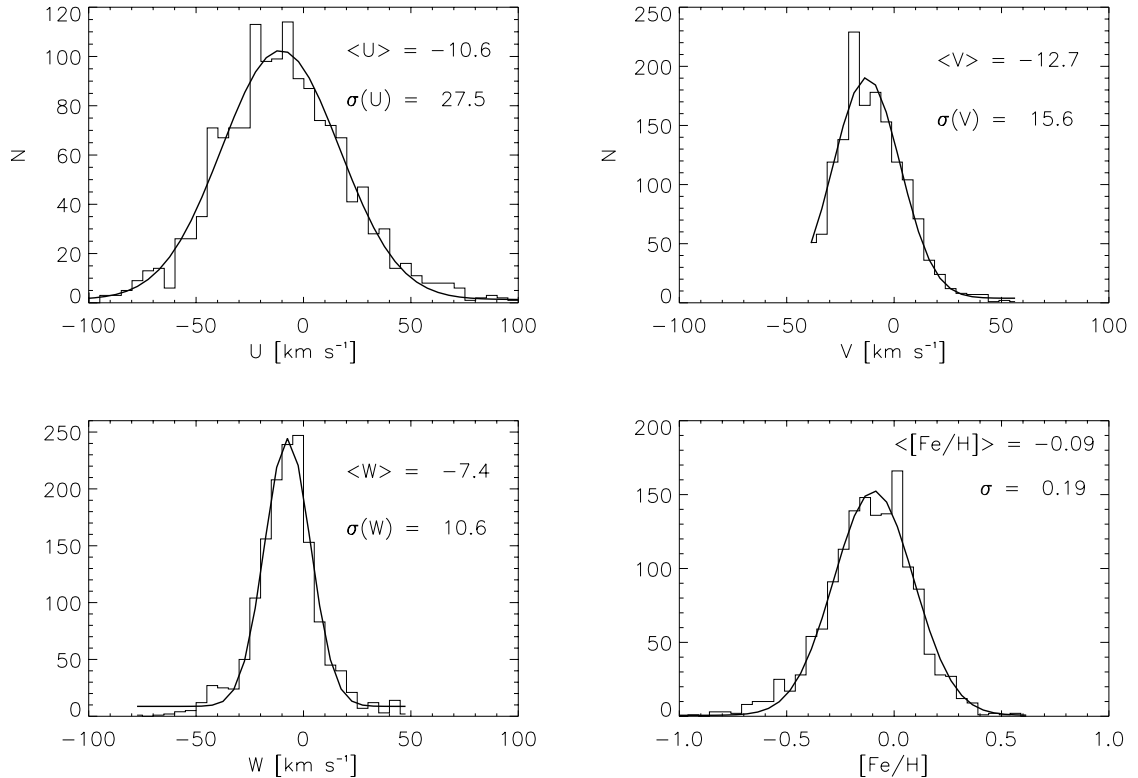


Fig. 17. Velocity and metallicity histograms of the stars in our extended sample within the region $V > -40$ and $-80 < W < +50$ km s⁻¹. The expected contamination by thick disk and halo populations is very small, and therefore we identify the observed distributions with the thin disk.

of 0.19 dex. This width is obviously convolved with the measurement errors. In this particular case, given the very inhomogeneous character of the Cayrel de Strobel et al. catalog, offsets between the metallicity scales of different authors are expected to contribute significantly to the observed width, yet, it is virtually identical to the estimates from the S⁴N sample.

We can repeat the fit to velocities of the thin disk stars in our extended sample for which we have kinematics, but not spectroscopic metallicities. The results for those stars within 100 pc – a restriction imposed in order to contain the errors in the astrometry – are in good agreement with those derived from the more restricted sample, as shown in Fig. 18. The Gaussian distributions become a poorer model for the observed distributions.

We can conclude that our sample of stars within 14.5 pc is representative, kinematically and chemically, of a much larger volume of the local thin disk.

6.2. On the peculiarity of the solar abundance ratios

The distributions of the Si, Sc, and Ti abundance ratios relative to iron at solar metallicity show a positive offset with respect to the solar ratios. Even if we restrict the comparison to stars with atmospheric parameters close to solar, this offset remains. It is difficult to attribute this to systematic errors. Our sky spectrum, obtained with the same instrumentation and setup as the stellar spectra, is in very good agreement with a smoothed version (to compensate for the higher spectral resolution) of the solar flux atlas of Kurucz et al. (1984). The solar analysis is

identical to the stellar analysis, except that the atmospheric parameters for the Sun were not derived in the same manner as for the stars. However, this is unlikely to induce such a shift in the abundances of different elements. Therefore we are inclined to suggest that the Sun is probably deficient in these elements compared to its immediate neighbors. This situation may also apply to O, Ca, Y, La, Ce and Nd.

Edvardsson et al. (1993) found a similar effect but when they restricted the comparison to stars with the same “birth galactocentric distance” and age as the Sun the differences turned out to be insignificant. Most stars in our sample, however, have solar-like (or thin-disk like) kinematics, so if their orbits are integrated most of them will give similar galactocentric distances at birth. A second issue is age. The Sun has an age in the middle of the age distribution for the stars in Edvardsson et al. sample, and the density of stars was roughly constant at all ages, but the sample is afflicted with severe selection effects.

Most of the stars in our very local (S⁴N) sample are still relatively close to the zero age main sequence (ZAMS) and therefore, we cannot derive ages for them by the methods described in Sect. 3.1.3. Figure 19 displays a histogram of the ages derived for the stars for which a 2- σ precision of 0.5 dex or better could be achieved in our extended sample (see Sect. 6). The age distribution covers from 0.16 Gyr (log Age \sim 8.2) to 10 Gyr, with a major concentration at \sim 1 Gyr. This result is in qualitative agreement with the results of Chereul et al. (1999) and Feltzing et al. (2001). Interpretation of this distribution is a major task and falls outside the scope of this paper. We refer the reader to the recent papers by Bertelli & Nasi (2001),

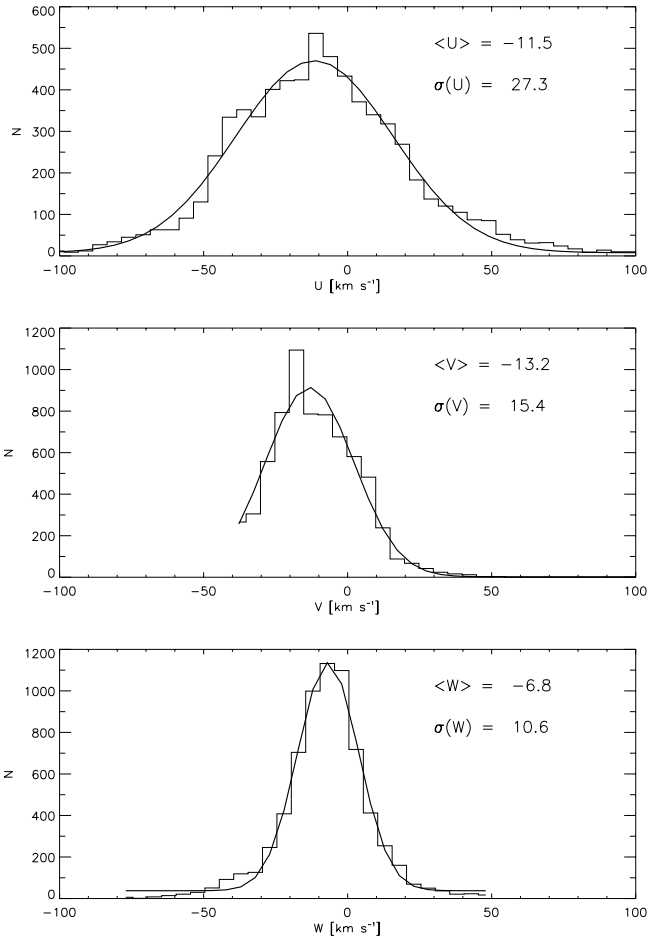


Fig. 18. Velocity histograms of the stars within 100 pc from the Sun in the extended sample for which astrometry and radial velocities, but not necessarily spectroscopic metallicities, are available. The sample is further restricted to $V > -40$ and $-80 < W < +50$ km s⁻¹ to exclude halo and thick disk stars.

Binney et al. (2002), and Vergely et al. (2002). The key fact that we will highlight is that the Sun (log Age ~ 9.7) is among the oldest stars in our extended sample.

The S⁴N sample, we have seen, includes a number of stars which are older than the Sun. Being dominated by K-type dwarfs, it is natural old stars will appear preferentially in Fig. 13. K-type stars tend to be excluded from abundance studies, which prefer brighter targets with cleaner spectra. Thus, metal-rich K-type dwarfs which are ubiquitous in S⁴N are discriminated against in the extended sample. Selection effects, however, for G-type stars are most certainly less serious. Therefore, it is plausible that the G-type stars in S⁴N share the age distribution of the extended sample. Then, if the Sun is somewhat older than the other G-type dwarfs in S⁴N, this would provide an explanation for the low abundance ratios to iron of some elements. The peculiarity of the Sun would be limited to its age: older than most thin disk dwarfs.

7. Summary and conclusions

Our spectroscopic analysis of the closest stellar neighbors reveals several interesting features. The derived [Fe/H]

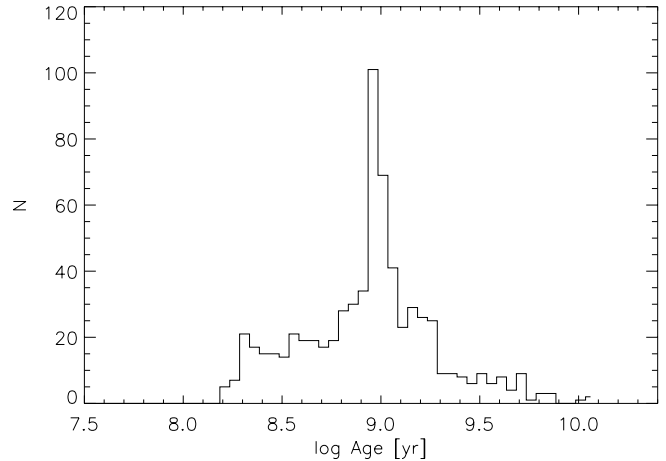


Fig. 19. Age histogram of the stars in the extended sample within the region $V > -40$ and $-80 < W < +50$ km s⁻¹ with $2\text{-}\sigma$ uncertainties smaller than 0.5 dex.

distribution for our sample is centered at $[\text{Fe}/\text{H}] \approx -0.1$, a value slightly higher than in most previous studies, which concentrated mainly on earlier spectral types. For a subsample of stars, comparison with evolutionary models can provide age estimates with moderate or small uncertainties. This reveals a number of metal-rich stars that appear to be as old as the most metal-poor stars in the sample (≥ 10 Gyr), and older than most solar-metallicity thin-disk stars. These old metal-rich stars show thin-disk kinematics, and disrupt a mild correlation between age and metallicity suggested by the stars with $[\text{Fe}/\text{H}] < 0$.

We find that our LTE abundance analysis does not satisfy the ionization balance for several elements. The discrepancies grow with metallicity, and appear to decrease with effective temperature, reaching extreme levels (nearly 0.5 dex) for the coolest and most metal-rich stars. Similar discrepancies were previously reported by Feltzing & Gustafsson (1998) for several K-type metal-rich field dwarfs as well as Schuler et al. (2003) and Yong et al. (2004) for K-type members of the open clusters M 34 and the Hyades, respectively. Systematic errors in the trigonometric gravities can be ruled out, as satisfying the ionization balance by modifying the gravity would require lower values by as much as 0.8 dex.

Systematic errors in the T_{eff} appear unlikely, as they would need upward revisions of up to ~ 300 K. We should emphasize that i) the sample of stars used by Alonso et al. (1996) to build the photometric calibrations employed here reach metallicities as high as $[\text{Fe}/\text{H}] = +0.5$ dex, covering adequately the range of (Fe I) abundances of our stars, ii) there is good agreement between the T_{eff} s derived from Strömgren photometry and the $(B - V)$ color index, and iii) the temperatures derived from the IRFM calibrations and from fitting the wings of Balmer lines are also in good agreement. The only requirement of the IRFM from model atmospheres is to correctly predict the IR continuum flux. The fact that fluxes for the stars used in the Alonso et al. calibrations were obtained with the Kurucz (1993) model atmospheres, which have been tested here and show the ionization imbalance, indicates an inconsistency between observations and the predictions of such models. We recall that

adopting other families of LTE line-blanketed homogeneous model atmospheres is of no help. The problem is probably connected to some of the assumptions involved in the modeling (maybe the *usual suspects*: LTE and surface convection). A direct comparison, however, of high-accuracy spectrophotometry with model fluxes should be carried out, before it is possible to definitely state that the inconsistencies are not related to uncertainties in the T_{eff} scale. Further study of open clusters, double, and multiple systems will help to clarify the source of the problem described.

Despite the the ionization problem, we use spectral lines of species that are dominant in K-type atmospheres to investigate abundance ratios to iron for a number of chemical elements. Our study suggests that the α elements and Sc are enhanced relative to iron for metal-rich stars. In an analysis strictly differential to the Sun, we find that some elements' ratios to iron are higher than solar at $[\text{Fe}/\text{H}] = 0$. This effect is detected, for instance, for most α elements and amounts roughly to 0.1 dex. This fact could be connected to, if not explained by, the Sun being somewhat older than most other dwarfs with similar spectral types in the thin disk – a conclusion that we reach from examining an extended sample of *Hipparcos* stars with metallicities from the literature.

Our efforts to obtain high-quality spectra for a distance- and M_V -limited sample of stars, have resulted in the identification of some serious problems in classical abundance analyses, rather than the very accurate relative abundances we hoped for. The spectra used in this work have been placed in a public archive. We propose this dataset as a standard test for modeling techniques to pass before the retrieved abundances are to be fully trusted.

Acknowledgements. We are grateful to the staff at McDonald and La Silla Observatories, in particular David Doss, for their helpful and professional assistance. Comments from the referee, Thierry Forveille, and from Lennart Lindegren helped to improve contents and presentation. We have made extensive use of the *Hipparcos* catalog, NASA's ADS, and the SIMBAD databases. We gratefully acknowledge funds for this project from the NSF (grant AST-0086321 and AST03-07532), NASA (NAG5-13147 and NAG5-13175), the Robert A. Welch Foundation of Houston (Texas), and the Swedish Research Council.

Appendix A: Determination of stellar ages and surface gravities

We estimated ages for the stars in the sample by comparing the position in the $M_V - T_{\text{eff}}$ plane of the star with the isochrones published by Bertelli et al. (1994). Our method is similar to that described by Reddy et al. (2003), but we have introduced some refinements. The procedure makes no assumption on the initial mass function, the metallicity distribution, or the star formation rate. The isochrones provide stellar properties such as M_V , T_{eff} , or $\log g$, as a function of three parameters: initial mass (M_i), age (Age), and metallicity (Z/Z_\odot). We start out by adopting flat distribution functions for those three parameters in the range:

$$\begin{aligned} 0.6 < M_i < 4.2 \\ 6.6 < \log \text{Age} < 10.2 \\ -1.65 < \log (Z/Z_\odot) < 0.35. \end{aligned} \quad (3)$$

Iron abundances were translated to metal mass fractions assuming $\log (Z/Z_\odot) = [\text{Fe}/\text{H}]$, and therefore we use them interchangeably below. Adopting a Gaussian probability density for T_{eff} , M_V , and $[\text{Fe}/\text{H}]$ centered at the measured values

$$\begin{aligned} P(T_{\text{eff}}, M_V, [\text{Fe}/\text{H}]) \propto & \exp \left[- \left(\frac{T_{\text{eff}} - T_{\text{eff}}^*}{\sqrt{2}\sigma(T_{\text{eff}})} \right)^2 \right] \\ & \times \exp \left[- \left(\frac{M_V - M_V^*}{\sqrt{2}\sigma(M_V)} \right)^2 \right] \exp \left[- \left(\frac{[\text{Fe}/\text{H}] - [\text{Fe}/\text{H}]^*}{\sqrt{2}\sigma([\text{Fe}/\text{H}])} \right)^2 \right] \end{aligned} \quad (4)$$

we determine the probability density distribution for the age

$$P(\log \text{Age}) = \iint P(T_{\text{eff}}, M_V, [\text{Fe}/\text{H}]) dM_i d[\text{Fe}/\text{H}]. \quad (5)$$

In practice, to find the best age estimate for each star, we discretized the problem by sampling the isochrones of Bertelli et al. with constant steps of $0.006 M_\odot$ in the initial mass M_i , 0.05 in $\log \text{Age}$ (Age in years), and 0.125 in $[\text{Fe}/\text{H}]$. We took advantage of a further simplification to speed up the calculation: the Gaussian component for $[\text{Fe}/\text{H}]$ in Eq. (4) was replaced by a boxcar with a width of 0.25 dex after checking that this introduced negligible differences. We then converted the integral in Eq. (5) into a sum over the area confined by an ellipsoid centered at the adopted values of T_{eff} , M_V , and $[\text{Fe}/\text{H}]$, with semi-axes three times the estimated $1-\sigma$ uncertainties in these parameters. From the probability distribution we find the mean and 1σ limits for the age of a star.

Similarly, the probability density for the surface gravity is derived

$$\begin{aligned} P(\log g) = & \iiint \log g P(T_{\text{eff}}, M_V, [\text{Fe}/\text{H}]) \\ & \times dM_i d[\text{Fe}/\text{H}] d \log \text{Age}. \end{aligned} \quad (6)$$

The isochrones employed do not consider enhancements in the abundances of the α elements for metal-poor stars. More realistic relations should take this into account, but as we are mainly concerned with thin disk stars, it will have no effect on our analysis.

Appendix B: Determination of UVW velocities

From the observed radial velocities (V_R), proper motions ($\mu_\alpha^* \equiv \mu_\alpha \cos \delta$, μ_δ), and parallaxes (π), velocities in a cylindrical galactic system are readily obtained (e.g., Johnson & Soderblom 1987)

$$\begin{pmatrix} U \\ V \\ W \end{pmatrix} = \mathbf{TA} \begin{pmatrix} V_R \\ k\mu_\alpha^*/\pi \\ k\mu_\delta/\pi \end{pmatrix} \quad (7)$$

where $k = 4.740470446$ is the astronomical unit in km s^{-1} , the matrix

$$\begin{aligned} \mathbf{A} = & \begin{pmatrix} \cos \alpha & \sin \alpha & 0 \\ \sin \alpha & -\cos \alpha & 0 \\ 0 & 0 & -1 \end{pmatrix} \\ & \begin{pmatrix} \cos \delta & 0 & -\sin \delta \\ 0 & -1 & 0 \\ -\sin \delta & 0 & -\cos \delta \end{pmatrix}, \end{aligned} \quad (8)$$

and the matrix \mathbf{T} is a function of the equatorial position of the galactic North Pole, and the position angle defining the zero of the galactic longitude

$$\mathbf{T} = \begin{pmatrix} \cos \theta_0 & \sin \theta_0 & 0 \\ \sin \theta_0 & -\cos \theta_0 & 0 \\ 0 & 0 & 1 \end{pmatrix} \begin{pmatrix} -\sin \delta_{\text{NGP}} & 0 & \cos \delta_{\text{NGP}} \\ 0 & -1 & 0 \\ \cos \delta_{\text{NGP}} & 0 & \sin \delta_{\text{NGP}} \end{pmatrix} \begin{pmatrix} \cos \alpha_{\text{NGP}} & \sin \alpha_{\text{NGP}} & 0 \\ \sin \alpha_{\text{NGP}} & -\cos \alpha_{\text{NGP}} & 0 \\ 0 & 0 & 1 \end{pmatrix}. \quad (9)$$

As all *Hipparcos* astrometry is given in the ICRS system J1991.25 (TT), we use $\alpha_{\text{NGP}} = 192.85948$ deg, $\delta_{\text{NGP}} = 27.12825$ deg, and $\theta_0 = 122.93192$ deg (ESA 1991; vol. 1)¹⁴, and therefore \mathbf{T} becomes the transpose of A_G (Eq. (1.5.11)) given in the *Hipparcos* catalog.

The *Hipparcos* catalog provides estimates of the variances and covariances for the astrometric parameters. We can therefore improve Johnson & Soderblom's estimates of the error bars in the galactic velocities by considering them. Given the input parameters

$$\mathbf{x} = (\alpha \ \delta \ \pi \ \mu_\alpha^* \ \mu_\delta \ V_R)^T. \quad (10)$$

The 6×6 covariance matrix is adopted from the *Hipparcos* catalog

$$C_{ii} = \sigma_i^2 \quad C_{ij} = \sigma_i \sigma_j \rho_{ij} \quad (11)$$

except for $\sigma(V_R)$, which is taken as the standard deviation when multiple measurements are available, or 2 km s^{-1} otherwise, and the covariance matrix of the galactic velocities is calculated

$$\mathbf{J} \mathbf{C} \mathbf{J}^T \quad (12)$$

where \mathbf{J} is the Jacobian of the transformation in Eq. (7)

$$\mathbf{J} = \begin{pmatrix} \partial U / \partial \alpha & \partial U / \partial \delta & \dots & \partial U / \partial V_R \\ \partial V / \partial \alpha & \partial V / \partial \delta & \dots & \partial V / \partial V_R \\ \partial W / \partial \alpha & \partial W / \partial \delta & \dots & \partial W / \partial V_R \end{pmatrix} = \mathbf{T} \mathbf{F} \quad (13)$$

and

$$\begin{aligned} F_{11} &= \sin \alpha (k \mu_\delta / \pi \sin \delta - V_R \cos \delta) - k \mu_\alpha^* / \pi \cos \alpha \\ F_{12} &= -V_R \cos \alpha \sin \delta - k \mu_\delta / \pi \cos \alpha \cos \delta \\ F_{13} &= k / \pi^2 (\mu_\alpha \sin \alpha + \mu_\delta \cos \alpha \sin \delta) \\ F_{14} &= -k / \pi \sin \alpha \\ F_{15} &= -k / \pi \cos \alpha \sin \delta \\ F_{16} &= \cos \alpha \cos \delta \\ F_{21} &= -\cos \alpha (k \mu_\delta / \pi \sin \delta - V_R \cos \delta) - k \mu_\alpha^* / \pi \sin \alpha \\ F_{22} &= -V_R \sin \alpha \sin \delta - k \mu_\delta / \pi \sin \alpha \cos \delta \\ F_{23} &= k / \pi^2 (-\mu_\alpha \cos \alpha + \mu_\delta \sin \alpha \sin \delta) \\ F_{24} &= k / \pi \cos \alpha \\ F_{25} &= -k / \pi \sin \alpha \sin \delta \\ F_{26} &= \sin \alpha \cos \delta \\ F_{31} &= 0 \\ F_{32} &= V_R \cos \delta - k / \pi \mu_\delta \sin \delta \\ F_{33} &= -k / \pi^2 \mu_\delta \cos \delta \\ F_{34} &= 0 \\ F_{35} &= k / \pi \cos \delta \\ F_{36} &= \sin \delta. \end{aligned} \quad (14)$$

The uncertainties in μ_α^* and μ_δ provided in *Hipparcos* are defined regarding the reference direction (α , δ) as fixed. Therefore, the derivatives of the velocity components with respect to the direction need not be considered, and the matrix elements F_{11} , F_{12} , F_{21} , F_{22} , F_{31} and F_{32} should be exactly zero. The standard errors (σ_i) and correlation coefficients (ρ_{ij}) involving α can be substituted by those for $\alpha^* \equiv \alpha \cos \delta$ (provided in the *Hipparcos* catalog), and $\sigma_\alpha \equiv \sigma(\alpha) \simeq \sigma(\alpha^*) / \cos \delta$. Use of Eq. (12) instead of that given by Johnson & Soderblom produces non-negligible differences in the estimated uncertainties in the galactic velocities, which generally become smaller for nearby *Hipparcos* stars.

References

- Allende Prieto, C. 2001, *ApJ*, 547, 200
Allende Prieto, C. 2002a, The Spectrum of the Th-Ar Hollow-Cathode Lamp Used with the 2dcoudé Spectrograph, McDonald Observatory Technical Note
<http://hebe.as.utexas.edu/2dcoude/thar/>
Allende Prieto, C. 2002b, *Rev. Mex. Astron. Astrofís., Conf. Ser.*, 10, 205
Allende Prieto, C. 2003, *MNRAS*, 339, 1111
Allende Prieto, C., & García López, R. J. 1998, *A&AS*, 131, 431
Allende Prieto, C., Ruiz Cobo, B., & García López, R. J. 1998, *ApJ*, 502, 951
Allende Prieto, C., Asplund, M., Barklem, P. S., & Ruiz Cobo, B. 2001a, *ApJ*, 558, 830
Allende Prieto, C., Lambert, D. L., & Asplund, M. 2001b, *ApJ*, 556, L63
Allende Prieto, C., Asplund, M., García López, R. J., & Lambert, D. L. 2002a, *ApJ*, 567, 544
Allende Prieto, C., Lambert, D. L., & Asplund, M. 2002b, *ApJ*, 573, L137
Allende Prieto, C., Beers, T. C., Li, Y., et al. 2003, in the *Carnegie Observatories Astrophys. Ser., Origin and Evolution of the Elements*, ed. A. McWilliam & M. Rauch (Pasadena: Carnegie Observatories), 4
Alonso, A., Arribas, S., & Martínez-Roger, C. 1996, *A&A*, 313, 873

¹⁴ The corresponding angles for B1950 are $(\alpha_{\text{NGP}}, \delta_{\text{NGP}}, \theta_0) = (192.25, 25.4, 123)$ deg (Johnson & Soderblom 1987). For J2000, the angles given for J1991.25 can be used with a negligible error (e.g. Murray 1989)

- Alonso, A., Arribas, S., & Martínez-Roger, C. 1999a, *A&AS*, 140, 261
- Alonso, A., Arribas, S., & Martínez-Roger, C. 1999b, *A&AS*, 139, 335
- Asplund, M., Gustafsson, B., Kiselman, D., & Eriksson, K. 1997, *A&A*, 318, 521
- Asplund, M., Grevesse, N., Sauval, A. J., Allende Prieto, C., & Kiselman, D. 2004, *A&A*, 417, 751
- Barbier-Brossat, M., & Figon, P. 2000, *A&AS*, 142, 217
- Barklem, P. S., & O'Mara, B. J. 1997, *MNRAS*, 290, 102
- Barklem, P. S., Piskunov, N., & O'Mara, B. J. 2000a, *A&A*, 355, L5
- Barklem, P. S., Piskunov, N., & O'Mara, B. J. 2000b, *A&A*, 363, 1091
- Barklem, P. S., Piskunov, N., & O'Mara, B. J. 2000c, *A&AS*, 142, 467
- Barklem, P. S., Stempels, H. C., Allende Prieto, C., et al. 2002, *A&A*, 385, 951
- Bertelli, G., Bressan, A., Chiosi, C., Fagotto, F., & Nasi, E. 1994, *A&AS*, 106, 275
- Bertelli, G., & Nasi, E. 2001, *AJ*, 121, 1013
- Binney, J., Dehnen, W., & Bertelli, G. 2000, *MNRAS*, 318, 658
- Blackwell, D. E., Lynas-Gray, A. E., & Smith, G. 1995, *A&A*, 296, 217
- Blackwell, D. E., & Shallis, M. J. 1977, *MNRAS*, 180, 177
- Bodaghee, A., Santos, N. C., Israelian, G., & Mayor, M. 2003, *A&A*, 404, 715
- Buzzoni, A., Chavez, M., Malagnini, M. L., & Morossi, C. 2001, *PASP*, 113, 1365
- Cayrel de Strobel, G., Soubiran, C., & Ralite, N. 2001, *A&A*, 373, 159
- Chen, Y. Q., Zhao, G., Nissen, P. E., Bai, G. S., & Qiu, H. M. 2003, *ApJ*, 591, 925
- Chereul, E., Crézé, M., & Bienaymé, O. 1999, *A&AS*, 135,
- Chiappini, C., Matteucci, F., & Gratton, R. 1997, *ApJ*, 477, 765
- Clausen, J. V., Baraffe, I., Claret, A., & Vandenberg, D. A. 1999, *Stellar Structure: Theory and Test of Connective Energy Transport*, ASP Conf. Ser., 173, 265
- Cunha, K., Smith, V. V., Suntzeff, N. B., et al. 2002, *AJ*, 124, 379
- Dehnen, W., & Binney, J. J. 1998, *MNRAS*, 298, 387
- Delhaye, J. 1965, *Stars and Stellar Systems*, vol. V: Galactic Structure, ed. A. Blaauw & M. Schmidt (Chicago: Univ. of Chicago Press), 61
- Dravins, D., & Nordlund, Å. 1990a, *A&A*, 228, 184
- Dravins, D., & Nordlund, Å. 1990b, *A&A*, 228, 203
- Edvardsson, B., Andersen J., Gustafsson, B., et al. 1993, *A&A*, 275, 101
- Eggen, O. J. 1960, *MNRAS*, 120, 430
- Eggen, O. J. 1998, *AJ*, 115, 2397
- ESA 1997, *The Hipparcos and Tycho Catalogues*, ESA SP-1200
- Favata, F., Micela, G., & Sciortino, S. 1997a, *A&A*, 324, 998
- Favata, F., Micela, G., & Sciortino, S. 1997b, *A&A*, 323, 809
- Feltzing, S., Bensby, T., & Lundström, I. 2003, *A&A*, 397, L1
- Feltzing, S., & Gonzalez, G. 2001, *A&A*, 367, 253
- Feltzing, S., & Gustafsson, B. 1998, *A&AS*, 129, 237
- Feltzing, S., & Holmberg, J. 2000, *A&A*, 357, 153
- Feltzing, S., Holmberg, J., & Hurley J. R. 2001, *A&A*, 377, 911
- Fekel, F. C., & Beavers, W. I. 1983, *ApJ*, 267, 682
- Flynn, C., & Morell, O. 1997, *MNRAS*, 286, 617
- Fuhrmann, K. 1998, *A&A*, 338, 161
- Gliese, W., & Jahreiß, H. 1991, *3rd Cat. of Nearby Stars*. Ast. Rechen-Inst, Heidelberg (CNS3)
- Griffin, R., & Griffin, R. 1979, *A Photometric Atlas of the Spectrum of Procyon $\lambda\lambda 3140-7470$ Å* (Cambridge: Institute of Astronomy, Observatories)
- Gustafsson, B., Bell, R. A., Eriksson, K., & Nordlund, Å. 1975, *A&A*, 42, 407
- Gustafsson, B., Karlsson, T., Olsson, E., Edvardsson, B., & Ryde, N. 1999, *A&A*, 342, 426
- Halbwachs, J. L., Mayor, M., Udry, S., & Arenou, F. 2003, *A&A*, 397, 159
- Harmanec, P. 1998, *A&A*, 335, 173
- Hauck, B., & Mermilliod, M. 1998, *A&AS*, 129, 431
- Haywood, M. 2001, *MNRAS*, 325, 1365
- Haywood, M. 2002, *MNRAS*, 337, 151
- Haywood, J. W., Hegyi, D. J., & Gudehus, D. H. 1992, *ApJ*, 392, 172
- Henry, L., Vardya, M. S., & Bodenheimer, P. 1965, *ApJ*, 142, 84
- Hinkle, K., Wallace, L., Valenti, J., & Harmer, D. 2000, *Visible and Near Infrared Atlas of the Arcturus Spectrum 3727-9300 Å* (San Francisco: ASP)
- Holweger, H., Kock, M., & Bard, A. 1995, *A&A*, 296, 233
- Johnson, D. R. H., & Soderblom, D. R. 1987, *AJ*, 93, 864
- Kaufer, A., Stahl, O., Tubbesing, S., et al. 2000, *Proc. SPIE*, 4008, 459
- Koch, A., & Edvardsson, B. 2002, *A&A*, 381, 500
- Kornilov, V. G., Volkov, I. M., Zakharov, A. I., et al. 1991, *Trudy Gosud. Astron. Sternberga*, 63, 4
- Kornilov, V., Mironov, A., & Zakharov, A. 1996, *Baltic Astron.*, 5, 379
- Kotoneva, E., Flynn, C., Chiappini, C., & Matteucci, F. 2002, *MNRAS*, 336, 879
- Kovtyukh, V. V., Soubiran, C., Belik, S. I., & Gorlova, N. I. 2003, *A&A*, 411, 559
- Kupka, F., Piskunov, N., Ryabchikova, T. A., Stempels, H. C., & Weiss, W. W. 1999, *A&AS*, 138, 119
- Kurucz, R. L. 1993, *ATLAS9 Stellar Atmosphere Programs and 2 km/s grid*, Kurucz CD-ROM No. 13
- Kurucz, R. L., Furenlid, I., Brault, J., & Testerman, L. 1984, *National Solar Observatory Atlas (Sunspot, New Mexico: NSO)*
- Lastennet, E., Fernandes, J., Valls-Gabaud, D., & Oblak, E. 2003, *A&A*, 409, 611
- Lawler, J. E., Wickliffe, M. E., den Hartog, E. A., & Sneden, C. 2001, *ApJ*, 563, 1075
- Malaroda, S., Levato, H., & Galliani, S. 2001, *VizieR Online Data Catalog*, 3216
- Malinie, G., Hartmann, D. H., Clayton, D. D., & Mathews, G. J. 1993, *ApJ*, 413, 633
- Mansour, N. B., Dinneen, T., Young, L., & Cheng, K. T. 1989, *Phys. Rev. A*, 39, 5762
- Mason, B. D., Henry, T. J., Soderblom, D. R., & Hartkopf, W. I. 2003, *Am. Astron. Soc. Meet.*, 203
- McWilliam, A. 1998, *AJ*, 115, 1640
- Mishenina, T. V., Kovtyukh, V. V., Soubiran, C., Travaglio, C., & Busso, M. 2002, *A&A*, 396, 189
- Murray, C. A. 1989, *A&A*, 218, 325
- Nissen, P. E. 1981, *A&A*, 97, 145
- Nissen, P. E., Primas, F., Asplund, M., & Lambert, D. L. 2002, *A&A*, 390, 235
- Nordlund, Å., & Dravins, D. 1990, *A&A*, 228, 155
- Oinas, V. 1974, *ApJS*, 27, 405
- Perrin, M. N., Cayrel, R., & Cayrel de Strobel, G. 1975, *A&A*, 39, 97
- Perrin, M.-N., Cayrel de Strobel, G., & Dennefeld, M., 1988, *A&A*, 191, 237
- Peterson, R. C., Dalle Ore, C. M., & Kurucz, R. L. 1993, *ApJ*, 404, 333
- Prochaska, J. X., & McWilliam, A. 2000, *ApJ*, 537, L57
- Reddy, B. E., Tomkin, J., Lambert, D. L., & Allende Prieto, C. 2003, *MNRAS*, 340, 304
- Reid, I. N. 2002, *PASP*, 114, 306
- Ribas, I. 2003, *A&A*, 398, 239
- Rocha-Pinto, H. J., & Maciel, W. J. 1996, *MNRAS*, 279, 447
- Rocha-Pinto, H. J., & Maciel, W. J. 1998a, *A&A*, 339, 791

- Rocha-Pinto, H. J., & Maciel, W. J. 1998b, MNRAS, 298, 332
- Ryan, S. G. 1998, A&A, 331, 1051
- Sandage, A., Lubin, L. M., & Vandenberg, D. A. 2003, PASP, 115, 812
- Shchukina, N., & Trujillo Bueno, J. 2001, ApJ, 550, 970
- Schwarzschild, M. 1958, in *Stellar Populations*, ed. D. J. K. O'Connell, *Specola Astronomica Vaticana*, 5, 300
- Schuler, S. C., King, J. R., Fischer, D. A., Soderblom, D. R., & Jones, B. F. 2003, AJ, 125, 2085
- Simmerer, J., Sneden, C., Ivans, I. I., et al. 2003, AJ, 125, 2018
- Spinrad, H. 1966, PASP, 78, 367
- Spinrad, H., & Taylor, B. J. 1969, ApJ, 157, 1279
- Stehlé, C., & Hutcheon, R. 1999, A&AS, 140, 93
- Taylor, B. J. 1970, ApJS, 22, 177
- Taylor, B. J. 2002, MNRAS, 329, 839
- Thóren, P., & Feltzing, S. 2000, A&A, 363, 692
- Torres, G., & Ribas, I. 2002, ApJ, 567, 1140
- Tull, R. G., MacQueen, P. J., Sneden, S., & Lambert, D. L. 1995, PASP, 107, 251
- Twarog, B. A. 1980, ApJ, 242, 242
- Twarog, B. A., Anthony-Twarog, B. J., & Tanner, D. 2002, AJ, 121, 2715
- van den Bergh, S. 1962, AJ, 67, 486
- Wolf, V. M., Tomkin, J., & Lambert, D. L. 1995, ApJ, 453, 660
- Woolley, R. 1965, *Stars and Stellar Systems*, vol. V: Galactic Structure, ed. A. Blaauw and M. Schmidt, (Chicago: Univ. of Chicago Press), 85
- Yong, D., Lambert, D. L., Allende Prieto, C., & Paulson, D. 2004, ApJ, 603, 697